ACSNANO

www.acsnano.org

ARTICLE

[2,1,3]-Benzothiadiazole-Spaced Co-Porphyrin-Based Covalent Organic Frameworks for O_2 Reduction

Subhajit Bhunia, Armando Peña-Duarte, Huifang Li, Hong Li, Mohamed Fathi Sanad, Pranay Saha, Matthew A. Addicoat, Kotaro Sasaki, T. Amanda Strom, Miguel José Yacamán, Carlos R. Cabrera, Ram Seshadri, Santanu Bhattacharya, Jean-Luc Brédas, and Luis Echegoyen*

Cite This: *ACS Nano* 2023, 17, 3492−3505

Read Online

ACCESS | Metrics & More | Article Recommendations | Supporting Information

ABSTRACT: **Designing N-coordinated porous single-atom catalysts (SACs) for the oxygen reduction reaction (ORR) is a promising approach to achieve enhanced energy conversion due to maximized atom utilization and higher activity. Here, we report two Co(II)-porphyrin/ [2,1,3]-benzothiadiazole (BTD)-based covalent organic frameworks (COFs; Co@*rhm*-PorBTD and Co@*sql*-PorBTD), which are efficient SAC systems for O_2 electrocatalysis (ORR). Experimental results demonstrate that these two COFs outperform the mass activity (at 0.85 V) of commercial Pt/C (20%) by 5.8 times (Co@*rhm*-PorBTD) and 1.3 times (Co@*sql*-PorBTD), respectively. The specific activities of Co@*rhm*-PorBTD and Co@*sql*-PorBTD were found to be 10 times and 2.5 times larger than that of Pt/C, respectively. These COFs also exhibit larger power density and recycling stability in Zn−air batteries compared with a Pt/C-based air cathode. A theoretical analysis demonstrates that the combination of Co-porphyrin with two different BTD ligands affords two crystalline porous electrocatalysts having different d-band center positions, which leads to reactivity differences toward alkaline ORR. The strategy, design, and electrochemical performance of these two COFs offer a pyrolysis-free bottom-up approach that avoids the creation of random atomic sites, significant metal aggregation, or unpredictable structural features.**

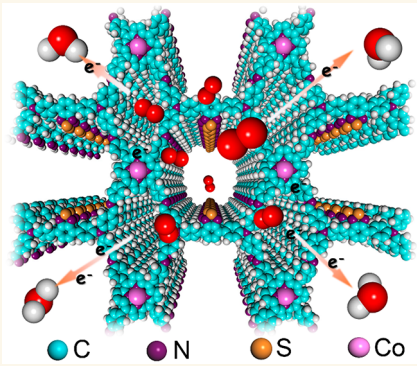

KEYWORDS: *covalent organic framework, donor−acceptor, benzothiadiazole based, porphyrinic framework, alkaline oxygen reduction, porphyrin-benzothiadiazole*

Among electrochemical conversion (EC) processes, the oxygen reduction reaction (ORR) is important for energy storage and conversion technologies due to its involvement in discharge processes in Li−O_2, Zn−air batteries, anion exchange membrane fuel cells (AEMFCs), and microbial fuel cells (MFCs).[1−3] Sluggish reaction kinetics often necessitate the use of platinum group noble metal (PGNM) catalysts, which makes the process expensive and inhibits the commercialization of fuel cell-powered automobiles. A US Department of Energy (DOE) report states that the use of a PGNM catalyst accounts for 55% of the cost of fuel cells for automobiles.[4] Several strategies have been adopted to replace PGNM with low-cost and highly active electrocatalysts including metal-free carbon materials (MFCMs),[5] single atom electrocatalysts (SAECs),[6,7] and metal alloys.[8] Among them, SAECs represent a bridge between homogeneous and heterogeneous electrochemical conversions in terms of maximum atom utilization, higher selectivity, robustness, and ease of integration in the electrodes.

To design an ideal SAEC, two factors need to be addressed carefully: (1) control over the position of single atomic sites with suitable local coordination environments and (2) fabrication of appropriate global supports that can participate in efficient electronic coupling with the metal sites. These are crucial parameters to control the activation barriers and mass transport kinetics. Reticular chemistry offers the opportunity to tailor the spacing between atomic sites precisely by using various ligands, which has a significant impact on the electro-

Received: October 3, 2022
Accepted: January 26, 2023
Published: February 8, 2023

Downloaded via UNIV OF TEXAS AT EL PASO on December 22, 2023 at 19:39:41 (UTC).
See https://pubs.acs.org/sharingguidelines for options on how to legitimately share published articles.

© 2023 American Chemical Society

https://doi.org/10.1021/acsnano.2c09838
ACS Nano 2023, 17, 3492−3505

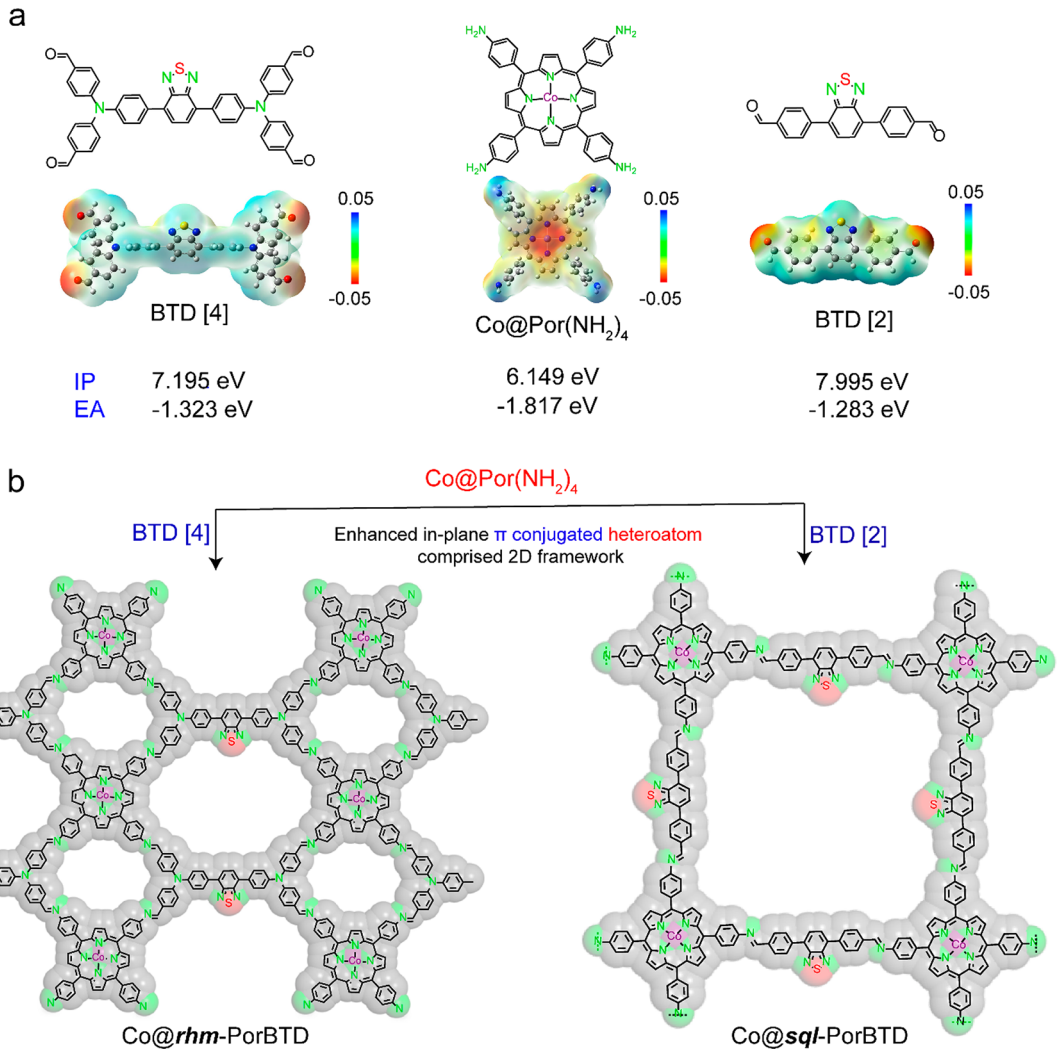

Figure 1. Structures of BTD [4], Co@Por(NH_2)$_4$, and BTD [2] with electrostatic potential (ESP) maps and computed value of ionization potentials (IP) and electron affinities (EA) for BTD [4], Co@Por(NH_2)$_4$, and BTD [2]. (b) Scheme of the synthesis of Co@*rhm*-PorBTD (left side) and Co@*sql*-PorBTD (right side) through [4 + 4] and [4 + 2] imine polycondensation, respectively.

kinetics.[9,10] Covalent organic frameworks (COFs)[11−19] and metal−organic frameworks (MOFs)[20−23] are materials that possess high porosity with atomically well-defined chemical environments and have a wide range of applications including gas separations/storage,[24−27] catalysis,[28,29] optoelectronics,[30,31] and energy storage.[32,33] Single atom-based COFs could address existing challenges for developing ideal SAECs based on their diverse reticular designs. The ability to define the spacing between atomic sites using different synthetic building units (SBUs) as spacers also makes the strategy attractive.[34,35] The in-plane extensive π delocalization and out-of-plane $\pi-\pi$ alignment of COF monolayers can potentially enhance charge transport inside crystals.[36,37] The emergence since 2015 of redox-active porphyrinic COFs and MOFs as SAECs has advanced the fields of CO_2 reduction reaction (CO_2RR),[38−40] hydrogen evolution reaction (HER)[41,42] oxygen evolution reaction (OER),[43,44] ORR,[45,46] and Li-ion battery.[47] Phthalocyanine-containing organic frameworks with different linkage functionalities have also been used recently for various electrochemical conversion processes like CO_2RR[48] and N_2 reduction reaction (NRR).[49,50]

Here, we report two Co (II) porphyrinic frameworks (Co@*rhm*-PorBTD and Co@*sql*-PorBTD) possessing different 2,1,3-benzothiadiazole (BTD)-based synthetic building units as linkers between Co (II) porphyrinic sites that are present inside the framework. These two cobalt-based SAEC exhibited excellent electrocatalytic efficiencies toward ORR. Due to the large electron affinity (Figure 1a), introducing BTD-based ligands as spacer groups between metalloporphyrin moieties results in enhanced intermolecular charge transfer pathways[51,52] along the crystalline porous channels.

RESULT AND DISCUSSION

Structural Characterization. Co@*sql*-PorBTD was synthesized by the imine condensation of 5,10,15,20-tetrakis(4-aminophenyl)-21*H*,23*H*-porphin cobalt(II) (Co@Por(NH_2)$_4$), 18 mg, 25 μmol) and 4,4′-(benzo[*c*][1,2,5]-thiadiazole-4,7-diyl)dibenzaldehyde (BTD [2], 16 mg, 50 μmol) (Figure 1b, right), and Co@*rhm*-PorBTD was synthesized by the condensation between Co@Por(NH_2)$_4$ (18 mg, 25 μmol) and 4,4′,4″,4‴-((benzo[*c*][1,2,5] thiadiazole-4,7-diylbis(4,1 phenylene)) bis-(azanetriyl))-tetrabenzaldehyde (BTD [4], 18 mg, 25 μmol) (Figure 1b, left). Crystalline Co@*sql*-PorBTD was obtained in the presence of 8 M acetic acid (0.25 mL) using *o*-DCB/ethanol (4:1, 1.25 mL) as the solvent while crystalline Co@*rhm*-

https://doi.org/10.1021/acsnano.2c09838
ACS Nano 2023, 17, 3492−3505

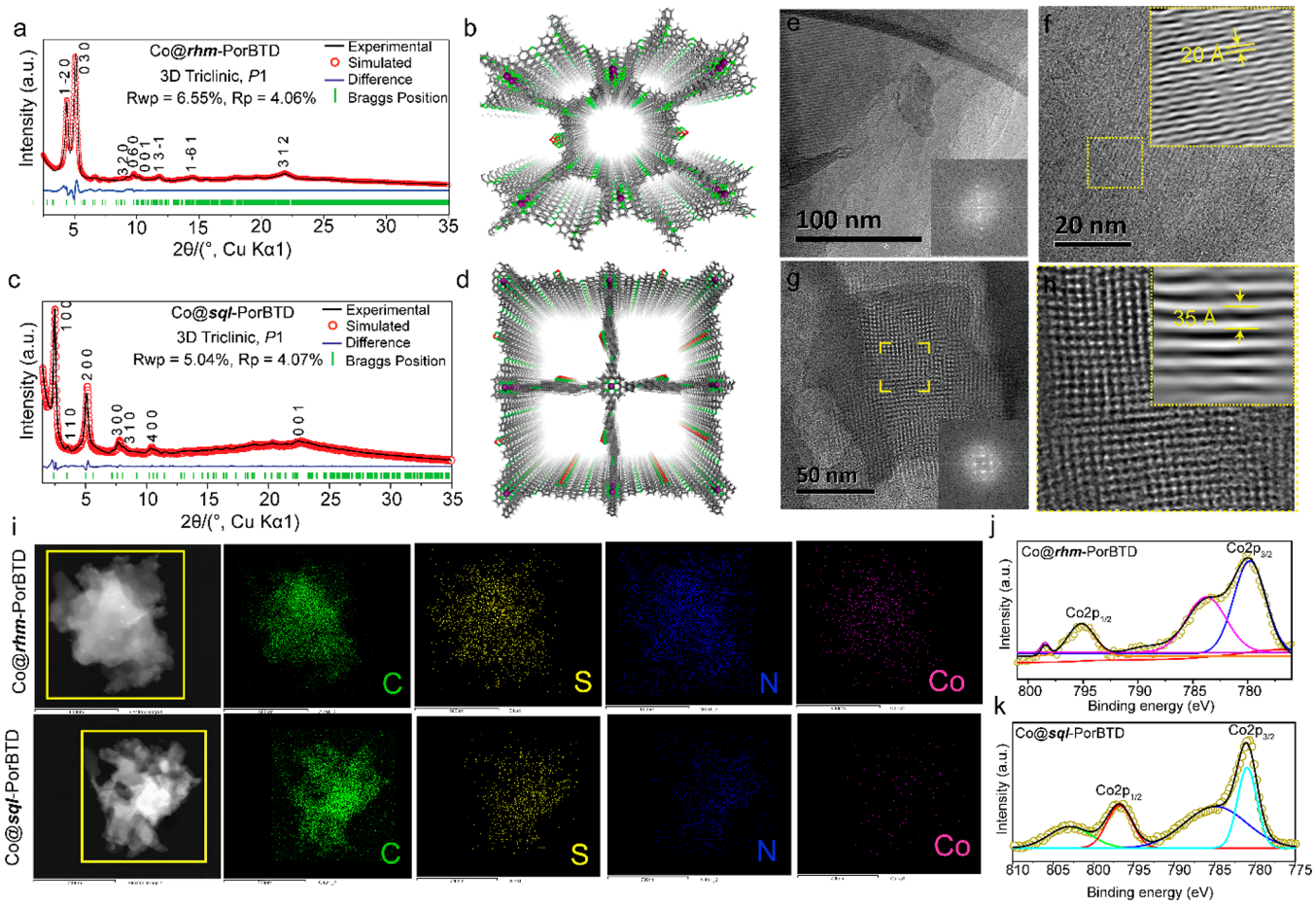

Figure 2. (a) Indexed experimental PXRD pattern for Co@*rhm*-PorBTD (black solid line), Pawley fitting (red circle plot), Bragg position (blue), and a difference plot (green). (b) Top views of the optimized structures of Co@*rhm*-PorBTD, showing an eclipsed (AA) structure. (c) Indexed experimental PXRD pattern for Co@*sql*-PorBTD (black solid line), Pawley fitting (red circle plot), Bragg position (blue), and a difference plot (green) for the optimized structure. (d) Top views of the optimized structures of Co@*sql*-PorBTD, showing an eclipsed (AA) structure. (e) HRTEM image (scale bar = 50 nm) for Co@*rhm*-PorBTD and FFT pattern (inset). (f) HRTEM image (scale bar = 20 nm) for Co@*rhm*-PorBTD and inverse FFT (inset) of the selected zone for the calculation of interplanar distance. (g) HRTEM image of Co@*sql*-PorBTD (scale bar = 50 nm) and FFT pattern (inset). (h) Magnified view of Figure 2g and the inverse FFT (inset) for the calculation of interplanar distance. (i) Energy-dispersive X-ray spectroscopy elemental mapping image (the yellow rectangle is the selected area in (i), scale bar = 600 nm. Co 2p XPS results for (j) Co@*rhm*-PorBTD and (k) Co@*sql*-PorBTD.

PorBTD was obtained in the presence of 10 M acetic acid (0.3 mL) using 1:1 *o*-DCB/*n*-butanol (1:1; 2 mL) as a solvent. The crystallinity of Co@***rhm***-PorBTD and Co@***sql***-PorBTD was achieved through several optimization processes, (Tables S1 and S2) like solvent and catalyst amounts (details are given in the Supporting Information, Section S2). Prolonged reaction times were needed for Co@***rhm***-PorBTD (7 days) while Co@***sql***-PorBTD crystallization occurred within 3 days (Figures S4 and S5). Co@***rhm***-PorBTD possesses a tessellated structure due to the use of the vertex elongated linker (BTD [4]), while Co@***sql***-PorBTD possesses a square lattice due to the polycondensation between the porphyrin-based square neutral structure and the linear BTD [2] linker.

Fourier transform infrared spectra (Figure S6) showed peaks located at 1599 and 1602 cm^{-1} for Co@***sql***-PorBTD and Co@***rhm***-PorBTD, respectively, which are characteristic of the C═N stretching band along with a decrease of the C═O (1690 cm^{-1}) stretching band of BTD [2] and BTD [4]. The N—H (3217 cm^{-1}) stretching signal for Co@Por$(NH_2)_4$ also disappeared for the resulting COFs, demonstrating a quantitative condensation between the amine and aldehyde groups. ^{13}C solid-state nuclear magnetic resonance (CP-MAS) measurements were conducted to analyze the chemical composition of these two imine-based COFs. Co@***rhm***-PorBTD shows the characteristic signals of the imine carbon (—C═N—) at ∼157 ppm (Figure S7) and Co@***sql***-PorBTD shows the peak at ∼152 ppm (Figure S8). The signals at ∼118 and 112 ppm for Co@***rhm***-PorBTD can be assigned to the meso and α-pyrrolic carbons, respectively, which are present in the Co-porphyrin macrocycle. The signals at ∼121 and 118 ppm for Co@***sql***-PorBTD are also for α-pyrrolic and meso carbons, respectively. The peak at ∼151 ppm was assigned to the quaternary imine carbon present in the BTD moiety. The high crystallinity of Co@***rhm***-PorBTD and Co@***sql***-PorBTD was revealed by the presence of sharp diffraction peaks in the powder X-ray diffraction (PXRD) patterns. The experimental PXRD pattern of Co@***rhm***-PorBTD (Figure 2a) displays two dominant peaks at 4.3° and 5° and five other peaks at 9.23°, 9.65°, 10.14°, 11.77°, 14.43°, and 10.65° corresponding to hkl values of (1−2 0), (0 3 0), (0 6 0), (0 0 1), (1 3−1), (1−6 1), and (3 1 2), respectively, for the AA stacking mode only (Figure 2b and Figure S9). Co@***sql***-PorBTD exhibited eight

https://doi.org/10.1021/acsnano.2c09838
ACS Nano 2023, 17, 3492−3505

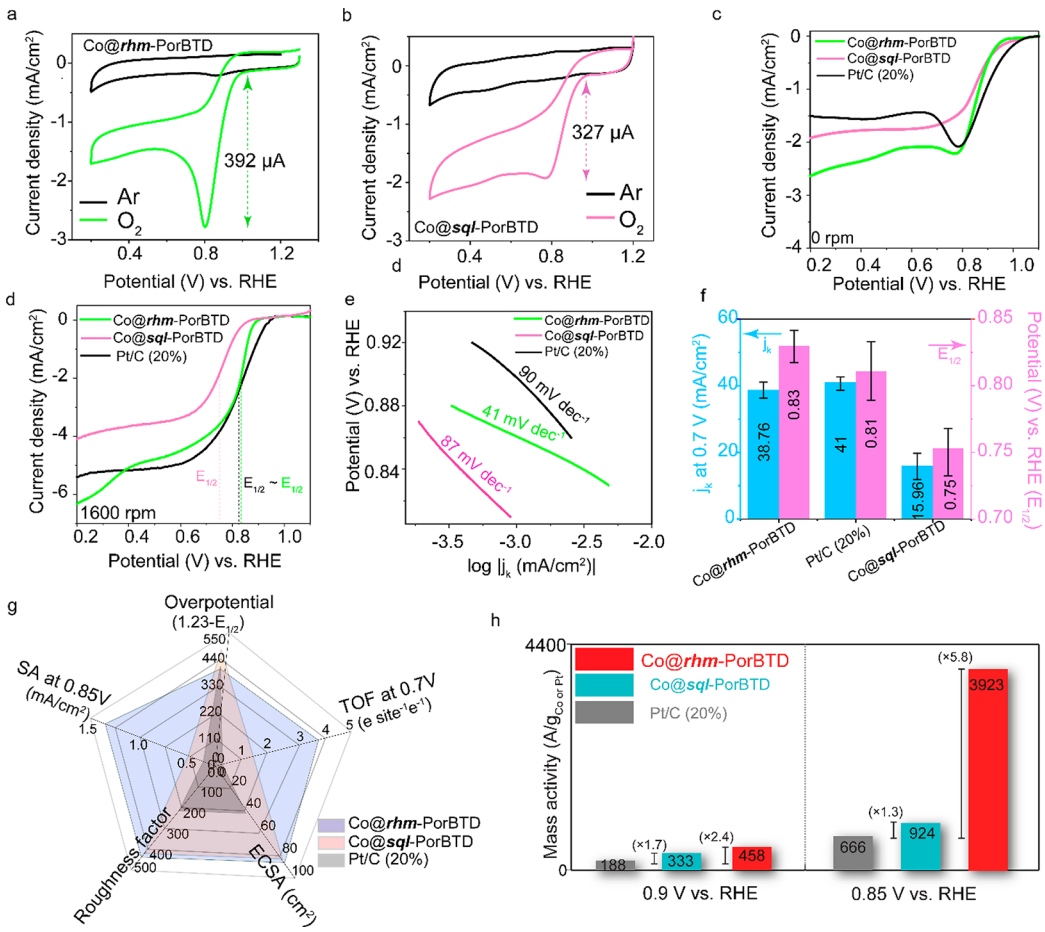

Figure 3. (a) CV curves for Co@*rhm*-PorBTD and (b) for Co@*sql*-PorBTD in 0.1 M KOH solution saturated with Argon (Ar) and O_2 at 10 mV/s respectively. (c) ORR polarization curve at an electrode rotation speed of 0 rpm and a scan rate of 10 mV s^{-1}. (d) ORR polarization curve at an electrode rotation speed of 1600 rpm and a scan rate of 10 mV s^{-1}. (e) Tafel plots for Co@*rhm*-PorBTD, Co@*sql*-PorBTD and Pt/C (20%). (f) Kinetic current density (at 0.7 V versus RHE) and half-wave potentials for Co@*rhm*-PorBTD, Co@*sql*-PorBTD, and 20% Pt/C. (g) Comparison of ECSA, overpotential from the half-wave potential (1.23- $E_{1/2}$), specific activities (0.85 V vs RHE), roughness factors, and turnover frequencies (0.7 V vs RHE) for Co@*rhm*-PorBTD, Co@*sql*-PorBTD, and 20% Pt/C. (h) Comparison of mass activities at 0.9 and 0.85 V versus RHE for these catalysts and for Pt/C (20%). The activities were calculated based on four independent measurements.

prominent diffraction peaks (Figure 2c), with the most-intensive one at 2.47° and seven other peaks at 3.51°, 5.1°, 7.74°, 8.33° 10.43°, and 22.67°, corresponding to hkl values of (1 0 0), (1 1 0), (2 0 0), (3 0 0), (3 1 0), (4 0 0), and (0 0 1), respectively, for the AA stacking mode only (Figure 2d and Figure S11). Pawley refinements of the experimental PXRD data showed good agreement with satisfactory residue values, (R_{wp}, R_p) of (6.55%, 4.06%) for Co@*rhm*-PorBTD and (R_{wp}, R_p) of (5.04%, 4.07%) for Co@*sql*-PorBTD. The cell parameters were obtained after Pawley refinements using a P_1 space group: a = 31.293 Å, b = 53.506 Å, c = 8.633 Å, α = 90.085°, β = 88.305°, γ = 90.92° for Co@*rhm*-PorBTD and a = 34.008 Å, b = 34.008 Å, c = 7.383 Å, $\alpha = \beta = \gamma$ = 90° for Co@*sql*-PorBTD. The transmission electron microscopy (TEM) images for Co@*rhm*-PorBTD and Co@*sql*-PorBTD show the formation of crystalline and ordered structures. The high-resolution TEM (HR-TEM) image of Co@*rhm*-PorBTD (Figure 2e,f) exhibits orderly oriented crystalline planes. The calculated interplanar distance for [1−2 0] from the inverse FFT pattern of the selected zone of the particular image was found to be ∼2 nm (Figure S13a,c), which matches the PXRD profile for the AA stacking. The HR-TEM image of Co@*sql*-PorBTD confirms the square lattice structure for the crystalline framework seen in the raw TEM image (Figure 2g,h). The calculated interplanar distance for [1 0 0] from the inverse FFT pattern of the selected zone of the particular image was found to be ∼3.5 nm (Figure S13b,d), which matches the PXRD profile results. Energy-dispersive X-ray spectroscopy (EDS) mapping analysis (Figure 2i) shows that carbon (C), nitrogen (N), sulfur (S), and cobalt (Co) are uniformly distributed for Co@*rhm*-PorBTD and Co@*sql*-PorBTD. The total Co contents for Co@*rhm*-PorBTD and Co@*sql*-PorBTD were determined to be 3.04 and 2.31 wt % by inductively coupled plasma optical emission spectrometry (ICP-OES). X-ray photoelectron spectroscopy (XPS) measurements were carried out (Figures S14 and S15) to determine the oxidation state of the cobalt for Co@*rhm*-PorBTD and Co@*sql*-PorBTD. They indicated that the coordinated metal centers for Co@*rhm*-PorBTD and Co@*sql*-PorBTD are in the +2 state (Figure 2j,k).

Co@*rhm*-PorBTD and Co@*sql*-PorBTD exhibit significant porosity with C, N, S, and Co atoms, which are homogeneously distributed over the imine framework. N_2 adsorption−desorption analyses were carried out at 77 K to

https://doi.org/10.1021/acsnano.2c09838
ACS Nano 2023, 17, 3492−3505

determine the porosities of the Co@*rhm*-PorBTD (Figure S16) and Co@*sql*-PorBTD (Figure S17) COFs. The Brunauer–Emmett–Teller (BET) surface areas for Co@*rhm*-PorBTD and Co@*sql*-PorBTD are 1960 and 650 m^2 g^{-1}, respectively. The pore size distribution for Co@*rhm*-PorBTD was derived from nonlinear density functional theory (NLDFT), which shows a bimodal porosity centered at 1.6 and 1.8 nm. Pore size distribution for Co@*sql*-PorBTD was similarly derived from NLDFT with the pore diameter estimated to be 3.5 nm, which is exactly the value from the PXRD results.

O_2 Electroreduction Activity and Stability. The oxygen reduction efficiency for both COFs was investigated by cyclic and linear sweep voltammetric (CV and LSV) analyses. CVs were recorded using a three-electrode system for both catalysts using an O_2-saturated electrolyte (0.1 M KOH). A strong O_2 reduction peak was observed at ∼0.8 V vs a reversible hydrogen electrode (RHE) for Co@*rhm*-PorBTD and Co@*sql*-PorBTD upon O_2 saturation of the electrolyte (Figure 3a,b). Upon closer inspection, Co@*rhm*-PorBTD shows a slightly positive shift (32 mV) compared to Co@*sql*-PorBTD in terms of the peak position for O_2 electroreduction. The O_2 reduction current was estimated to be 392 and 327 μA for Co@*rhm*-PorBTD and Co@*sql*-PorBTD, respectively, whereas the universally used 20% Pt/C (20 wt % platinum on Vulcan XC-72R) shows a value of 140 μA (Figure S20). Being nonprecious metal systems,[53] Co@*rhm*-PorBTD and Co@*sql*-PorBTD showed an almost twice larger reduction current than commercial 20% Pt/C, which is utilized as the ORR standard reference.[54,55]

LSV curves were recorded under static and dynamic conditions for both COFs (Figure 3c,d). Figure 3d presents the ORR polarization curves for the COFs and for 20% Pt/C in 0.1 M KOH under rotating conditions. The rotating disk electrode (RDE) experiment was done at 1600 rpm and a scan rate of 10 mV/s, following the US Department of Energy protocol.[56] Co@*rhm*-PorBTD and Co@*sql*-PorBTD showed onset potentials of ∼0.89 and 0.85 V (vs RHE) and half-wave potentials of 0.83 and 0.75 V (versus RHE), respectively, whereas Pt/C (20%) showed a slightly higher onset value shift (∼47 and 81 mV) compared with the values for Co@*rhm*-PorBTD and Co@*sql*-PorBTD. In addition, the $E_{1/2}$ value for Co@*rhm*-PorBTD was found to outperform that for Pt/C (20%) by 15 mV, whereas Co@*sql*-PorBTD showed a slightly lower $E_{1/2}$ (∼66 mV) shift than Pt/C (20%). The Tafel slopes were found to be 41 and 87 mV/dec for Co@*rhm*-PorBTD and Co@*sql*-PorBTD (Figure 3e), respectively; these values are much lower than for 20% Pt/C (90 mv/dec), demonstrating that the COF-based SACs exhibit faster ORR kinetics than Pt/C (20%). To probe the catalytic resistance, electrochemical impedance spectroscopy (EIS) measurements were carried out (Figure S21). Interestingly, the Nyquist plots demonstrate that Co@*rhm*-PorBTD exhibits a smaller charge-transfer resistance (34.4 Ω) than Pt/C (46.67 Ω) while Co@*sql*-PorBTD has a slightly higher R_{ct} (63.01 Ω). The kinetic current density (J_k) for Co@*rhm* PorBTD is 38.7 mA/cm^2 at 0.7 V, which is slightly lower than that for Pt/C (20%) (41 mA/cm^2) while Co@*sql*-PorBTD showed a current density of 15.9 mA/cm^2 (Figure 3f).

The ORR kinetics were further assessed by recording linear sweep polarization curves at different rotation speeds in the range 250–2500 rpm (Figures S22–S24). The Koutecky–Levich (K–L) equation was used for the rotating disc electrode (RDE) data (Pine Research Instrumentation) to analyze the mechanism at the COFs/electrolyte interfaces. The linearity of the plots indicates first-order electro-kinetics. The numbers of electrons involved in the electroreduction process were calculated from the slope of the K–L plot and found to be 3.93/O_2 molecule and 3.85/O_2 molecule for Co@*rhm*-PorBTD and Co@*sql*-PorBTD, respectively. The number of electrons transferred was also determined using the rotating ring disc electrode (RRDE) technique (Figures S25 and S26).

The intrinsic electroactivities were further investigated by calculating the overpotential from the half-wave potential (1.23 − $E_{1/2}$), electrochemical active surface areas (ECSAs), specific activities (SAs), roughness factors (RFs), and turnover frequencies (TOFs) (Figure 3g and Table S8). Before calculations, elemental analysis was done for electrocatalyst ink to estimate the actual cobalt loading on electrode surface (Table S7). In order to calculate ECSA, double layer capacitances (C_{dl}) were measured from the CVs in the nonfaradaic region. C_{dl} corresponds to half of the slope of the linear fit of Δj (at 1.05 V vs RHE) vs the scan rate plots (Figures S27–S29). ECSA was found to be 86 cm^2 for Co@*rhm*-PorBTD and 82.6 cm^2 for Co@*sql*-PorBTD; these values are nearly twice the value for commercial Pt/C (20%) (42 cm^2). Based on the crystal structures, the active site densities for Co@*rhm*-PorBTD and Co@*sql*-PorBTD were found to be 3.1×10^8 and 2.64×10^8 metal site/μm^3, respectively (Table S6). High valent connectedness of the [4 + 4] rhombus topology causes this high packing density over the square [4 + 2] topology. The role of atomic cobalt was assessed by investigating the ORR activity of COFs in 0.1 M KOH in the presence of axial ligation agents (KSCN and HMTA) that selectively poison Co–N sites,[57] whereas the N and S active centers are inert to SCN^- ions. As can be seen from Figure S30, the catalytic performance of Co@*rhm*-PorBTD was reduced significantly after the addition of 20 mM KSCN to the alkaline electrolyte. The significant decay of current density and overpotential can be attributed to the blocking of the cobalt centers by SCN^- or HMTA groups. It demonstrates that the cobalt atoms serve as the primary active sites for the O_2 electroreduction. The residual current density and O_2 reduction performance of the poisoned electrocatalysts arise from the large number of incorporated heteroatoms (not involved in ligand coordination) present in the highly porous Co@*rhm*-PorBTD (1960 m^2 g^{-1}) electrocatalyst.

The mass activity was calculated at 0.9 V vs RHE to compare Co@*rhm*-PorBTD and Co@*sql*-PorBTD with other previously reported systems. Co@*rhm*-PorBTD exhibits a mass activity of 458 A/g_{Co}, which is nearly 2.4 times larger than that for commercial Pt/C (20%), while Co@*sql*-PorBTD has a mass activity of ∼333 A/g_{Co}, which is nearly 1.7 times larger than that for Pt/C (20%, 188 A/g_{Pt}, Figure 3h). The MAs at 0.85 V for Co@*rhm*-PorBTD and Co@*sql*-PorBTD were measured to be 5.8 and 1.3 times (3.923 and 0.92 A mg_{Co}^{-1}, respectively) larger than the activity of Pt/C. The SA values for Co@*rhm*-PorBTD (1.32 mA cm^{-2}) and Co@*sql*-PorBTD (0.324 mA cm^{-2}) were found to be ∼10 and 2.5 times higher than for Pt/C (0.142 mA cm^{-2}), respectively. These activity values for nonprecious cobalt-based SACs exceed the 2020 US Department of Energy target value (440 A/g_{Pt}) for platinum.[58] The TOFs were calculated for Co@*rhm*-PorBTD to be 3.73 and 1.47 e $site^{-1}$ sec^{-1} for Co@*sql*-PorBTD. These values are considerably higher than that for commercial Pt/C (20%), 0.272 e $site^{-1}$ sec^{-1}. The stabilities of the electrocatalysts were

https://doi.org/10.1021/acsnano.2c09838
ACS Nano 2023, 17, 3492–3505

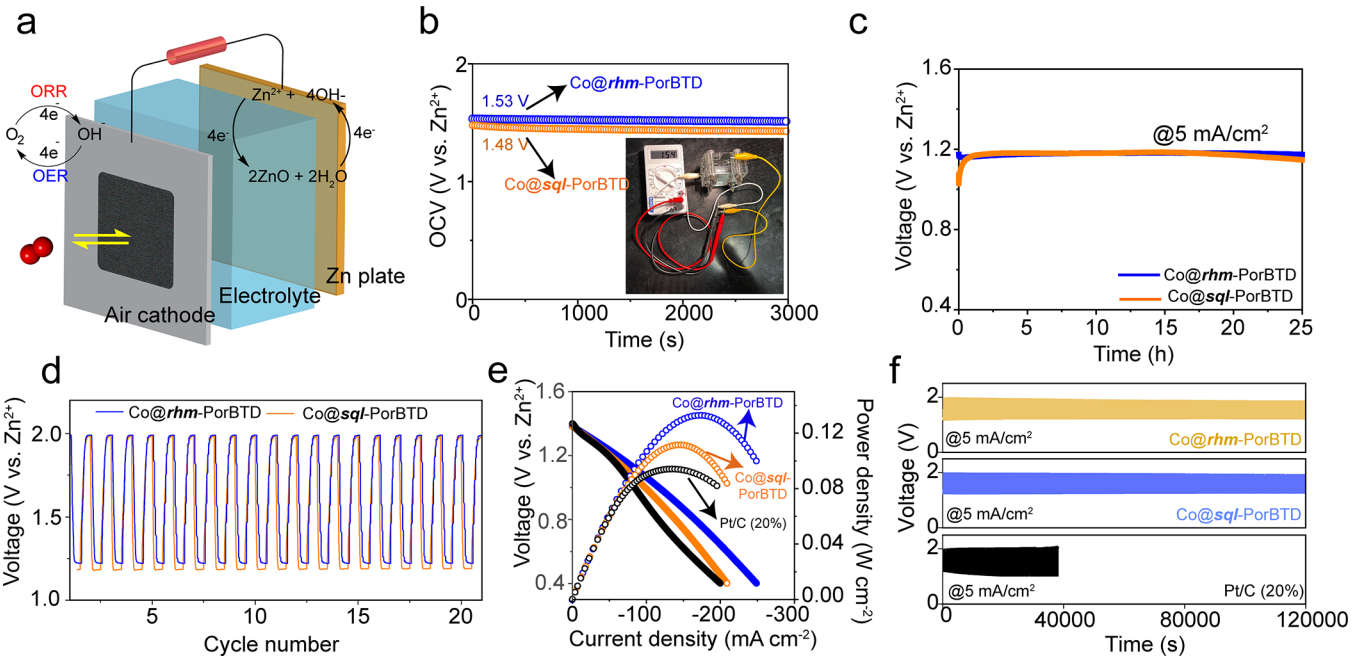

Figure 4. Zinc−air battery performance. (a) Schematic diagram of the homemade zinc−air battery. (b) Open circuit plot of the Zn−air battery using Co@*rhm*-PorBTD and Co@*sql*-PorBTD as a catalyst (inset: photograph of assembled zinc−air battery). (c) Discharge curves of Zn−air batteries using Co@*rhm*-PorBTD and Co@*sql*-PorBTD at current densities of 5 mA cm^{-2}. For each battery, a Zn plate was used as the anode, and 6 M KOH + 0.2 M Zn(OAc)$_2$ was used as the electrolyte. All the catalytic mass loadings were 0.25 mg cm^{-2}. (d) Discharge and charge cycling curves. (e) Comparison of polarization plot and power density plot using Pt/C (20%), Co@*rhm*-PorBTD, and Co@*sql*-PorBTD as cathodes. (f) Long-term discharge/charge cycling performance of Zn−air batteries with Co@*rhm*-PorBTD, Co@*sql*-PorBTD, and Pt/C (20%) at a current density of 5 mA cm^{-2}.

evaluated by rapid scanning between 0.2 and 1.1 V (vs RHE) up to 5000 cycles (Figures S32−S34). Co@*rhm*-PorBTD showed a negligible activity loss (3.1% loss) after 5000 cycles. Co@*sql*-PorBTD showed an MA value of 837 A/g_{Co} (2.4% loss) after 5000 cycles. Under the same conditions, commercial Pt/C (20%) showed an 9% activity loss after 5000 cycles (Figure S35). The mass activity and TOF values are much higher compared to many recently reported well-performing systems (Tables S9 and S10). Based on the presented results, Co@*rhm*-PorBTD and Co@*sql*-PorBTD are excellent examples of pyrolysis-free bottom-up synthetic systems for the precise design of (N, S) comprising single metal atom electrocatalysts. Several studies have demonstrated that an unsymmetric spin/charge distribution caused by doping with different electronegative atoms (N, S, P, *etc.*) in the basal and edge plane positions influences the O_2 electroreduction pathway.[59−62] The activities observed for the COFs also can be attributed to the fact that higher porosity provides better exposure of the active sites across the support and maximize the catalytic performance over that of Pt/C (20%).

The PXRD of the recovered electrocatalysts was also recorded after 5000 cycles and revealed that the crystallinity of the frameworks was retained after the prolonged alkaline electrocatalysis (Figures S36 and S37). The Co 2p XPS spectra showed that the Co retained the same valence state (Co^{2+}) before and after 5000 cycles (Figure S38). The SEM and TEM images (Figures S39 and S40) of Co@*rhm*-PorBTD and Co@*sql*-PorBTD agreed well with the morphology before ORR, indicating no particle or metal aggregation during ORR cycles. The tolerance to methanol crossover effects and the stability of the catalysts were investigated by chronoamperometric *I*−*t* experiments. Three molar methanol was introduced into the O_2 saturated electrolyte during the *I*−*t* experiments and no visible changes were observed for Co@*rhm*-PorBTD or Co@*sql*-PorBTD (Figure S41). In contrast, a significant ORR current drop was observed for Pt/C (20%). After a 24 h long run of chronoamperometric *I*−*t* experiments, a 19% current loss was observed for Co@*rhm*-PorBTD and 23% for Co@*sql*-PorBTD (Figure S42), which demonstrates the durability of these electrocatalysts compared to Pt/C (30% current loss).

Zinc−Air Battery Performance. The ORR and OER (Section S7) activities were further evaluated using Co@*rhm*-PorBTD and Co@*sql*-PorBTD as air cathodes for application in rechargeable zinc−air batteries. The COFs were coated on a carbon cloth and a battery cell was assembled using a Zinc plate as anode (Figure 4a and Figure S44). The cell testing was done in air instead of pure O_2. The Co@*rhm*-PorBTD-based cathode had a stable open circuit voltage of 1.53 V while Co@*sql*-PorBTD showed a value of 1.48 V (Figure 4b). The robustness of these COF-based cathodes was evaluated by long-term-discharge experiments. When a galvanostatic discharge was done at 5 mA/cm^2 for 25 h, no obvious voltage drop was observed for either COF (Figure 4c). Co@*rhm*-PorBTD exhibited charge−discharge voltages of 1.99 and 1.22 V and Co@*sql*-PorBTD exhibited values of 1.99 and 1.18 V, respectively (Figure 4d). The peak power densities for Co@*rhm*-PorBTD and Co@*sql*-PorBTD were found to be 138 and 117 mW cm^{-2}, respectively (Figure 4e) which were larger than for commercial Pt/C (20%) (96 mW cm^{-2}). A long-term galvanostatic charge/discharge was conducted for each system, and no significant performance loss was noted after 1000 cycles over 33 h. In contrast, the performance of Pt/C (20%) was significantly reduced after 100 cycles (Figure 4f), which

https://doi.org/10.1021/acsnano.2c09838
ACS Nano 2023, 17, 3492−3505

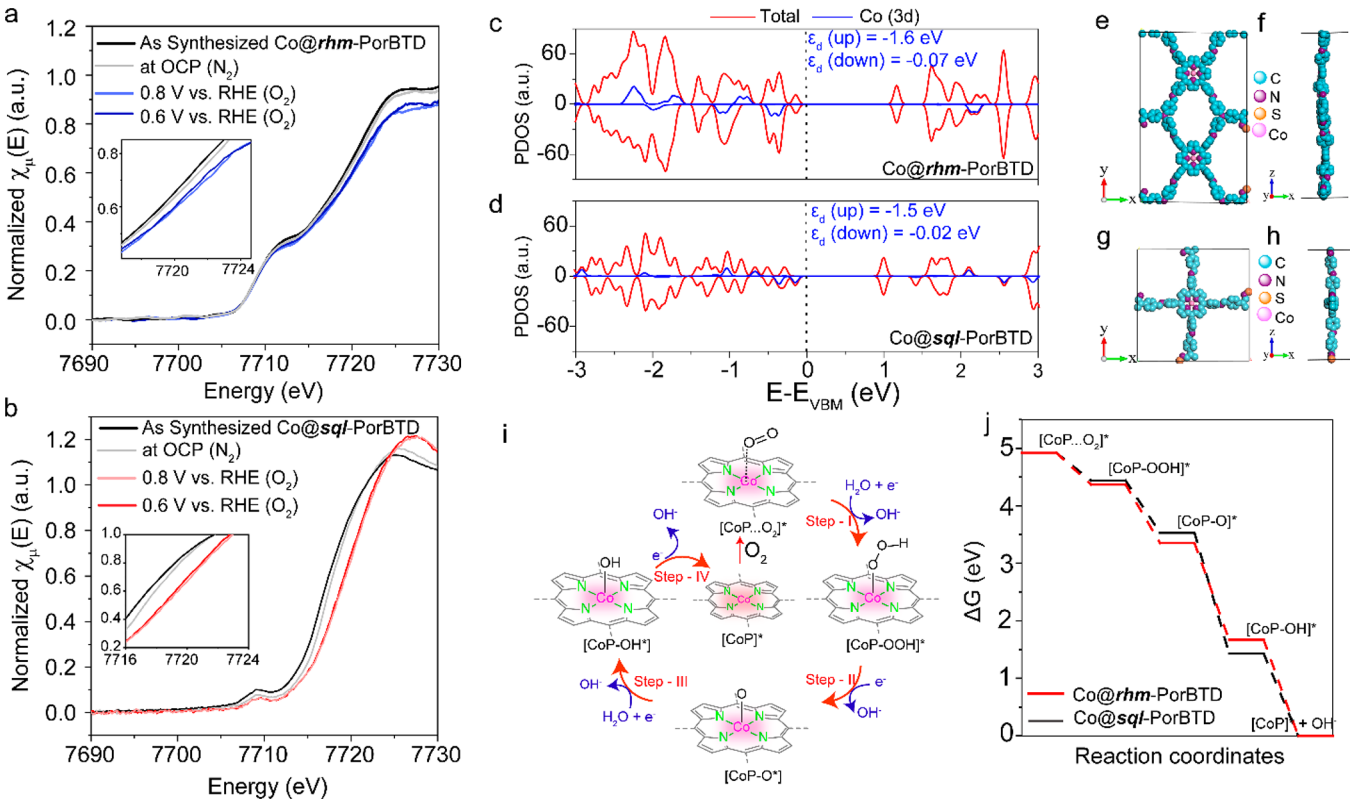

Figure 5. ***Ex situ*** **and** ***in situ*** **XANES characterization (inset: magnified view) of (a) Co@*rhm*-PorBTD and (b) Co@*sql*-PorBTD. Total density of states (red) and projected density of states to the cobalt 3d (blue) in (c) Co@*rhm*-PorBTD and (d) Co@*sql*-PorBTD. (e) Top view and (f) side view of the optimized Co@*rhm*-PorBTD monolayer. (g) Top view and (h) side view of the optimized Co@*sql*-PorBTD monolayer. (i) Proposed catalytic scheme for ORR by Co@*rhm*-PorBTD and Co@*sql*-PorBTD [CoP* denotes for activated cobalt porphyrin] and corresponding free energy diagram (j).**

demonstrates the superior stability of the COF-based air cathodes over that of commercial Pt/C (20%).

Operando **Co K-edge XANES/EXAFS and Theoretical Insights.** *Operando* Co K-edge XANES/EXAFS studies were performed to track the electronic structural changes of the cobalt site present in Co@***rhm***-PorBTD and Co@***sql***-PorBTD under precatalytic to catalytic conditions. Parts a and b of Figure 5 illustrate that all spectra possess a pre-edge transition peak (dipole forbidden 1s → 3d), which can be attributed to the square planar CoN_4 site of both catalysts (Figure S45a). *Ex situ* and *in situ operando* XAS were carried out to investigate the core structural changes of the active site under ORR bias. Surprisingly, XANES for Co@***rhm***-PorBTD and Co@***sql***-PorBTD under open circuit conditions are shifted toward higher energy from *ex situ* spectra, which can be attributed to the slight Co oxidation by electrolyte contact.[63,64] When the ORR potential (0.8 and 0.6 V vs RHE) was applied in the presence of O_2, the absorption edge spectra were shifted toward higher energy, which indicates electron transfer from the Co sites to oxygen and subsequent evolution of Co(III) species under ORR bias.[65,66] The valence state of Co was calculated, and it was found to be 2.6 and 2.2 for Co@***rhm***-PorBTD and Co@***sql***-PorBTD, respectively, under 0.6 V vs RHE (Figure S45d). The *in situ* EXAFS study showed that the ORR bias in the presence of oxygen leads to the elongation of the Co−N bond (Figure S45b,c), which could be attributed to the distortion of the square planar CoN_4 by oxygen-based adsorbates.[67]

Spin- polarized density functional theory (SP-DFT) calculations were performed to better understand the electronic structures and O_2 electroreduction activities of Co@***rhm***-PorBTD and Co@***sql***-PorBTD. The projected density of states (PDOS) to the Co d-bands and the position of the Co d-band center (ε_d) with reference to the valence band maximum (VBM) are shown in Figure 5c,d. The energetic position of the highest occupied d-bands for Co@***rhm***-PorBTD is about 0.2 eV lower than that for Co@***sql***-PorBTD. According to the PDOS (cobalt 3d), ε_d for Co@***rhm***-PorBTD was found to be more negative (−1.6 eV for spin-up and −0.07 eV for spin-down) than for Co@***sql***-PorBTD (−1.5 eV for spin-up and −0.02 eV for spin-down), which results in weaker adsorption of the ORR intermediates for Co@***rhm***-PorBTD compared to Co@***sql***-PorBTD. The weaker adsorption for Co@***rhm***-PorBTD results in faster ORR kinetics compared to Co@***sql***-PorBTD.[68] Free energy calculations for each step were performed to investigate the effect of the [2,1,3]-benzothiadiazole-based struts on the energetics for the ORR steps (Figure 5i,j, Table S5). The diagram shows that each step is exothermic and the rate-determining step (RDS) for Co@***rhm***-PorBTD and Co@***sql***-PorBTD is the first step that forms OOH* from O_2 with a stabilization energy of 550 and 480 meV, respectively. Therefore, this explains why Co@***rhm***-PorBTD is more efficient for the ORR reaction than Co@***sql***-PorBTD.

https://doi.org/10.1021/acsnano.2c09838
ACS Nano 2023, 17, 3492−3505

CONCLUSION

In summary, we have developed two Co(II)-porphyrin-based covalent organic frameworks, Co@***rhm***-PorBTD and Co@***sql***-PorBTD, that exhibit ORR mass activity, which outperform many previously reported platinum group catalysts. To the best of our knowledge, there are many reports of ORR applications with porphyrinic COFs that involve pyrolytic "top down" approaches. Our report demonstrates a "bottom-up" approach to producing ORR electrocatalysts. The spacing of the active sites was accomplished using different benzothiadiazole groups in order to introduce heteroatoms (N, S) inside the COF backbone. Overall, our results represent a proof-of-concept that demonstrates that the bottom-up design of COF frameworks, by using proper synthetic building units with a combination of suitable metal sites can achieve improved intrinsic electroactivity and maximum atom utilization. Topology-dependent high-density packing of active sites and their electronic coupling with global support can reduce the gap between homogeneous and heterogeneous electrocatalysts. The results demonstrate that nonprecious metal-based functional COFs are promising alternatives to replace the platinum group catalyst for ORR in alkaline environments. Our findings also represent a step forward in catalyst design by using reticular chemistry with various metal coordination functionalities to ultimately replace PGNM catalysts in the field of green energy conversion and storage.

METHODS

Chemicals. All starting materials and solvents were obtained from MilliporeSigma (Merck). 5,10,15,20-Tetrakis(4-aminophenyl) porphyrin was purchased from Frontier Scientific, Inc (Newark, DE). 2,1,3-Benzothiadiazole-4,7-bis(boronic acid pinacol ester), cobalt(II) chloride, and 4-bromotriphenylamine were purchased from MilliporeSigma (St. Louis, MO). Phosphorus(V) oxychloride was obtained from Fisher Scientific (Fair Lawn, NJ). 20% Platinum on Vulcan XC-72R was obtained from Fuelcell store (College Station, TX).

*Synthesis of Co@**rhm**-PorBTD.* A 10 mL glass ampule tube was charged with 5,10,15,20-tetrakis(4-aminophenyl)-21*H*,23*H*-porphin cobalt(II) (Co@Por$(NH_2)_4$) (36 mg, 50 μmol), BTD [4] (36 mg, 50 μmol), 1,2-dichlorobenzene (1 mL), *n*-butanol (1 mL), and 10 M aqueous acetic acid (0.3 mL), and the mixture was sonicated for 30 min. After sonication, the tube was flash frozen at 77 K (liquid N_2 bath) and a 3/4 freeze−pump−thaw cycle was conducted. Then, the system was evacuated and flame-sealed. The ampules were placed in an oven at 135 °C for 7 days, yielding a dark purple precipitate that was isolated by filtration and washed with methanol, dichloromethane, and acetone several times, and the powder emerged in *n*-hexane overnight, and finally, it was air-dried to produce Co@***rhm***-PorBTD in an isolated yield of 76%.

*Synthesis of Co@**sql**-PorBTD.* A 20 mL scintillation vial was charged with 5,10,15,20-tetrakis(4-aminophenyl)-21*H*,23*H*-porphin cobalt(II) (Co@Por$(NH_2)_4$) (36 mg, 50 μmol), BTD [2] (16 mg, 0.1 mmol), 1,2-dichlorobenzene (1 mL), ethanol (0.25 mL), and 8 M aqueous acetic acid (0.25 mL), and the mixture was tightly capped and sonicated for 1 h. After sonication, the vial was placed in an oil bath at 120 °C for 3 days, yielding a greenish-black precipitate that was isolated by filtration. The product was washed with methanol, dichloromethane, and acetone several times, and the powder emerged in *n*-hexane overnight. Finally, the precipitate was air-dried to produce Co@***sql***-PorBTD in an isolated yield of 87%.

Characterizations of Materials. The powder X-ray diffraction (PXRD) data were collected on a PANalytical B.V. Empyrean powder diffractometer using a Cu Kα source (λ = 1.5418 Å) over the range 2θ = 2.0−40.0° with a step size of 0.02° and 2 s per step. The N_2 adsorption/desorption analysis was done at 77 K using a Micromeritics 3Flex with micropore analysis capabilities. The Co@***rhm***-PorBTD and Co@***sql***-PorBTD samples were degassed at 120 °C for 8 h prior to analysis. To estimate pore size distributions, nonlocal density functional theory (NLDFT) was applied to analyze the N_2 isotherm based on the model of N_2 at 77K on carbon with slit pores and the method of non-negative regularization. High-resolution transmission electron microscopy (HRTEM) was done in a JEOL 2010 TEM microscope operating at an accelerating voltage of 200 kV. High-angle annular dark field scanning transmission electron microscopy (HAADF-STEM) mapping was carried out ultrahigh-resolution field-emission gun (UHR-FEG) TEM (JEM 2100 F, JEOL) using a 200 kV electron source. XPS analysis of Co@***rhm***-PorBTD and Co@***sql***-PorBTD were carried out by X-ray photoelectron spectroscopy (XPS, Omicron, model: 1712-62-11) method using an Al−Kα radiation source under 15 kV voltage and 5 mA current. A JEOL JEM-1230 transmission electron microscope with a Gatan Orius SC1000 side mount CCD camera at 120 kV was used for obtaining TEM images of the COFs. X-ray photoelectron spectroscopy (XPS) was conducted using a Thermo Scientific ESCALAB 250 Xi XPS system in which the analysis chamber pressure was 1.5×10^{-9} mbar and the size of the X-ray spot was 500 μm. FTIR spectra were recorded in the solid state using a Bruker Tensor 27 in transmittance mode. X-ray photoelectron spectroscopy (XPS) was carried out in an Omicron electron spectrometer, equipped with EA125 analyzer and Mg Kα X-ray source with a photon energy of 1253.6 eV. Cobalt content was quantified by inductively coupled plasma−optical emission spectrometry (ICP-OES) using a Varian Vista RL spectrometer. ^{1}H NMR spectra were recorded on a Bruker AVANCE III 400 MHz spectrometer. ^{1}H NMR spectra are referenced with respect to residual ^{1}H solvent peaks as internal standards or the characteristic ^{1}H peak of the solvent.

Electrochemical Measurements. Catalytic inks were prepared by suspending 3 mg COFs/acetylene black (1:1) in 1.0 mL of isopropanol/5% aqueous Nafion (37:1 v/v) solution and subsequently bath sonicated for approximately 6 h to get homogeneous dispersion (N.B. Carbon was just used as a conductive support since it cannot provide any active sites for 4e$^-$ ORR).[69] Ten microliters of the resulting ink was coated onto a polished glassy carbon (GC) electrode (S_{geo} = 0.196 cm^2) as the working electrode (WE) to achieve a loading of 0.15 mg/cm^2. The electrodes were dried under infrared lamp. The sample procedure was followed to maintain the same loading mass for Pt/C (20%). Ag/AgCl in saturated 3 M KCl solution was used as the reference electrode (RE), and a graphite rod was used as the auxiliary electrode (CE). The experimental potential was calibrated with the following equation-

$$E_{RHE} = E_{Ag/AgCl} + 0.197 + 0.059\ pH \quad (1)$$

All electrochemical ORR measurements were performed using a three-electrode system (CH 600E) and a pine modulated speed rotator (Pine Research Instrumentation, Inc.). ORR cyclic voltammetry (CV) was recorded in argon (Ar)/oxygen (O_2)-saturated 0.1 M KOH solution at room temperature at a scan rate of 50 mV/s. The linear polarization curve was recorded in O_2-saturated 0.1 M KOH solution at a scan rate of 10 mV s^{-1} and an electrode rotation speed of 0−2500 rpm. The durability test was carried out at 0.7 V vs RHE and 1600 rpm in O_2-saturated 0.1 M KOH solution. The kinetic parameters were estimated by applying the Koutecky−Levich (K−L) equations:

$$\frac{1}{j} = \frac{1}{j_L} + \frac{1}{j_k} = \frac{1}{B\omega^{1/2}} + \frac{1}{j_k} \quad (2)$$

$$B = 0.2nFC_0{D_0}^{2/3}\nu^{-1/6} \quad (3)$$

$$j_k = nFkC_0 \quad (4)$$

where j is the total current density, j_k and j_L are the kinetic and limiting current densities, respectively. ω is the angular velocity of the electrode, n is the number of electrons involved in the ORR process, F is the Faraday constant, C_0 is the bulk concentration of O_2 in

https://doi.org/10.1021/acsnano.2c09838
ACS Nano 2023, 17, 3492−3505

electrolyte (1.2×10^{-3} mol· L^{-1} for 0.1 M KOH), D_0 is the diffusion coefficient of O_2 (1.9×10^{-5} $cm^2 \cdot s^{-1}$ for 0.1 M KOH), ν is the kinetic viscosity of the electrolyte (0.01 cm s^{-1}), and k is the electron transfer rate constant. The constant 0.2 is adopted when the rotation speed is shown in revolutions per minute (rpm).

The mass activity was calculated by normalizing the kinetic current, extracted from the K−L equation to the mass loading of cobalt metals. CV profiles were obtained at 10 mV/s in Ar-saturated 0.1 M KOH. ORR polarization profiles were obtained in O_2-saturated 0.1 M KOH at 10 mV/s and 1600 rpm. Durability tests were carried out by potential cycling from 0.2 to 1.1 V at 50 mV/s for 5000 cycles in O_2-saturated 0.1 M KOH. The ORR profiles after 5000 cycles were measured in a fresh 0.1 M KOH solution to avoid potential contamination from dissolved metal species in the solution.

The Tafel slope is a key descriptor of the electro-kinetics of any electrochemical reaction (here, the oxygen reduction reaction) and it can be derived by the following equation:

$$\eta = a + \frac{2.3RT}{\alpha nF} \log j_k \tag{5}$$

where η, α, F, and j_k denote the overpotential, transfer coefficient, Faraday constant (96485 C mol^{-1}), and kinetic current density, respectively. n is the number of electrons involved in the electrochemical process. The Tafel slope is expressed as $b = \frac{2.3RT}{\alpha nF}$.

The electrochemically active surface area (ECSA) of Co@***rhm***-PorBTD, Co@***sql***-PorBTD, Pt/C (20%) were estimated by evaluating the cyclic voltammetry (CV) measurements in the nonfaradaic region (1−1.12 V vs RHE) in an O_2-saturated 0.1 M KOH solution at different scan rates (10, 20, 30, 40, 60, 80, and 100 mV/s). The difference between anodic and cathodic current densities (Δj, at 1.05 V vs RHE) were plotted against the scan rate to obtain a linearly fitted Δj. Electrochemical double-layer capacitance (C_{dl}) is estimated by taking the half value of the slope between fitted Δj vs scan rate. The ECSA was then calculated by using the following equation:

$$\text{ECSA} = \frac{C_{dl}}{C_S} \tag{6}$$

C_S is the specific capacitance of the electrode with a flat surface, which is found to be ∼35−40 μF cm^{-2}. The roughness factors (RFs) were calculated using the equation:

$$\text{RF} = (\text{ECSA})/(\text{geometric area of the electrode}) \tag{7}$$

The mass activity (MA) was calculated by the following equation:

$$\text{MA} = \frac{\text{background corrected kinetic current}(i_{k,\text{ink}} - i_{k,\text{additive C only}})}{\text{cobalt present in the electrode ink}} \tag{8}$$

where i_k is the kinetic current, which is calculated by multiplying J_k (derived from the above Koutecky−Levich equation at 0.9 and 0.85 V vs RHE, respectively, with the geometric area of glass carbon disk. Background corrected kinetic current (i_k) was estimated by subtracting the kinetic current for acetylene black only ($i_{k,\text{ additive C}}$, Figure S31) from the ink kinetic current ($i_{k,\text{ ink}}$).

Specific activity (SA) was derived from the MA by using the following equation:

$$\text{SA} = \frac{\text{MA}}{\text{ECSA}} \tag{9}$$

Turnover frequency calculation (TOF) was calculated as

$$\text{TOF} = \frac{\text{number of total } H_2O \text{ turnover}/cm^2(n_{O_2/H_2O})}{\text{total number of active site}/cm^2} \tag{10}$$

where N_A is the Avogadro number (6.023×10^{23} atoms/mol).

The total active site was calculated according to the amount of cobalt (wt %, ICP-OES) present in the electrocatalytic layer (0.15 mg/cm^2) in the glassy carbon electrode. EIS was measured in the frequency range from 10^6 to 1 Hz. Rotating ring-disk electrode (RRDE) experiment was carried using a RRDE component (AFE7R9, Pine Instruments) consisting of a glassy carbon rotating disk electrode (Φ = 5.5 mm) and a Pt ring (Φ = 6.5 mm) was used, with a theoretical collection efficiency of 37%. The hydrogen peroxide selectivity was calculated using the following equation:

$$\text{hydrogen peroxide yield (\%)} = \frac{I_{ring}/N}{|I_{disk}| + I_{ring}/N} \tag{11}$$

The number of electrons transferred on the disk electrode in the ORR process (n) was evaluated by using the equation:

$$n = 4 \times \frac{|I_{disk}|}{|I_{disk}| + I_{ring}/N} \tag{12}$$

where I_{ring} is the ring current, I_{disk} is the disk current, and N is the determined collection efficiency.

***Ex Situ* and *in Situ* X-ray Absorption Spectroscopy Electrochemical Experiments.** *Ex situ* and *in situ* X-ray absorption spectroscopy (XAS) experiments were conducted using 7-BM QAS NSLS-II beamline at the Brookhaven National Laboratory. The cobalt K-edge XANES data were recorded in fluorescence mode using a PIPS detector. *In situ* XAS was recorded using same beamline with a three-electrode electrochemical cell following the previously reported procedure.[70] Data calibration/processing, fittings, and normalization were done using the Demeter software package (ATHENA and ARTEMIS). All Co K-edge XANES spectra data were referenced to the Co foil data for which an E_0 value of 7709 eV was used.

Structural Simulation. Geometries of Co@***rhm***-PorBTD and Co@***sql***-PorBTD COFs were constructed using AuToGraFS[71] and optimized using UFF4MOF.[72,73] Then, the structure was finally refined using the GFN-xTB method.[74] All calculations were undertaken using AMS2022.[75] Pawley refinement was carried out using the Reflex module in Material studio version 7.0, a software package for crystal determination from XRD pattern. Unit cell parameters were kept unchanged to the theoretical value. The Pawley refinement was done to optimize the unit cell iteratively until convergence of the wR_p value. The pseudo-Voigt profile function was used for whole profile fitting, and Berar−Baldinozzi function was chosen for asymmetry correction during refinement processes. Crystallite size and lattice strain were also considered during ultrafine refinement.

Free Energy Calculations for ORR. Spin-polarized density functional theory (SP-DFT) calculations were carried out with the projector-augmented wave (PAW)[76] method as implemented in VASP.[77,78] The generalized gradient approximation functional of Perdew−Burke−Ernzerhof (PBE)[79] with dispersion corrections (Grimme DFT-D3)[80] was adopted in all calculations. The strong electron−electron Coulomb interactions that exist in the 3d electrons of the cobalt ions were captured by Hubbard (U) and exchange (J) constants. In the present calculations, U and J for the cobalt ions were taken to be 4 and 1 eV, respectively.[81] COF monolayers were built and separated by a vacuum space larger than 20 Å in the z direction (to prevent interactions among the monolayers). The plane-wave cutoff was set at 400 eV. A Γ-point only k-sampling was adopted in the geometry optimizations, and a 6 × 6 × 1 k-mesh generated by the Monkhorst−Pack scheme[82] was used for the self-consistent electronic-structure calculations. An energy convergence criterion of 10^{-6} eV was used, and the atomic positions were relaxed until the maximal force on each atom was smaller than 0.01 eV A^{-1}.

The d-band center, ε_d, defined as the average energy of the d-band electrons, was calculated using the projected d-band density of states[83]

$$\varepsilon_d = \frac{\int_{-\infty}^{0} E.\ \rho_d dE}{\int_{-\infty}^{0} \rho_d dE} \tag{13}$$

where ρ_d represents the projected d-band density of states and E is the energy of the corresponding state usually referenced to the Fermi level. We note that the COF monolayers investigated here are

https://doi.org/10.1021/acsnano.2c09838
ACS Nano 2023, 17, 3492−3505

semiconductors; as such, we took the valence band maximum as the reference.

The Gibbs reaction free energy change (ΔG) of each elementary step in ORR was evaluated based on the computational hydrogen electrode (CHE) model developed by Nørskov and co-workers.[84] We denote the free energies of the COF monolayer and the O-containing intermediates in the ORR four-electron pathway as G(CoP), G(CoP-OOH), G(CoP-O), and G(CoP-OH). The Gibbs free energy changes in the ORR steps were evaluated as

$$\Delta G(1) = G(\text{CoP-OOH}) - G(O_2) + G(\text{CoP}) + G(H_2)/2$$

$$\Delta G(2) = G(\text{CoP-O}) + G(H_2O) - G(\text{CoP-OOH}) + G(H_2)/2$$

$$\Delta G(3) = G(\text{CoP-OH}) - G(\text{CoP-O}) + G(H_2)/2$$

$$\Delta G(4) = G(\text{CoP}) + G(H_2O) - G(\text{CoP-OH}) + G(H_2)/2$$

The free energy of each individual system (G) was determined as

$$G = E + \text{ZPE} - \text{TS}$$

where E, ZPE, and TS correspond to the total energy from DFT calculations, zero-point energy, and entropic contributions (T was set at 298.15 K), respectively. The zero-point energies and thermal entropy corrections of the adsorbed intermediates were calculated using the VASPKIT code.[85] The TS values of molecular H_2O and H_2 were taken from a previous report.[86] The free energy of O_2(g) was derived as $G_{O_2\,(g)} = 2G_{H_2O\,(l)} - 2G_{H_2\,(g)} + 4.92$ eV, with 4.92 eV being the overall formation energy toward ORR.[87]

Single-Molecule Calculations. The geometries and electronic structures of COF subunits BTD [2], BTD [4], and Co@Por$(NH_2)_4$ were calculated at the density functional theory (DFT) level using the long-range corrected ωB97X-D functional[88] as implemented in the Gaussian 09 package.[89] The SDD basis set and corresponding effective core potential[90] were used for cobalt, and an all-electron 6-31G(d,p)[91,92] basis set was used for the other atoms. All the geometries were optimized without symmetry constraints and were confirmed as potential energy surface minima by harmonic vibrational frequency calculations. The vertical electron affinity (EA) and ionization potential (IP) were determined with the ΔSCF method on the basis of the neutral optimized structures and are defined as

$$\text{vertical EA} = E_{\text{radical-anion}} - E_{\text{neutral}}$$

$$\text{vertical IP} = E_{\text{radical-cation}} - E_{\text{neutral}}$$

where E_{neutral} represents the total energy of the optimized neutral molecule and $E_{\text{radical-anion}}$ and $E_{\text{radical-cation}}$ denote the total energies of the radical-anion and radical-cation based on the optimized structures of neutral molecules.

ASSOCIATED CONTENT

Supporting Information

The Supporting Information is available free of charge at https://pubs.acs.org/doi/10.1021/acsnano.2c09838.

Discussions of synthesis of ligands, calculation of theoretical number of active sites, oxygen evolution reaction, and zinc air battery, figures of ^{1}H NMR spectra for all compounds, optimization of solvent systems, FTIR spectra, ^{13}C solid-state CP-MAS NMR, PXRD patterns, slipped AA stacking and AB stacking, TEM images, interplanar distance of crystalline planes, XPS profiles, porosity analysis, N_2 adsorption−desorption isotherms, pore size distributions, EDS spectra, cobalt content, cyclic voltammetry, Nyquist plots LSV curves, K−L plot, RRDE voltammograms, mass activity versus cycle number, loss of crystallinity, SEM images, methanol resistance, chronoamperometric I−T measurement and durability test, Tafel plots, schematic diagram of assembled Zn−air battery, *ex situ* and *in situ* EXAFS, and oxidation state analysis by K-edge position fitting of XANES, and tables of synthesis of compounds under variable solvothermal conditions, unit-cell parameters and fractional atomic coordinates, calculated total energies and sum of zero-point energies and entropy corrections, density of catalytically active-sites, elemental composition of bulk COFs and COF-based formulation of catalyst inks, comparison of TOF, ECSA, roughness factor, MA, and SA for electrocatalysts, and comparison of the MA, SA, and TOF of Co@***rhm***-PorBTD and Co@***sql***-PorBTD with previously reported ORR catalysts (PDF)

AUTHOR INFORMATION

Corresponding Author

Luis Echegoyen − *Department of Chemistry and Biochemistry, The University of Texas at El Paso, El Paso, Texas 79968, United States;* orcid.org/0000-0003-1107-9423; Email: echegoyen@utep.edu

Authors

Subhajit Bhunia − *Department of Chemistry and Biochemistry, The University of Texas at El Paso, El Paso, Texas 79968, United States;* orcid.org/0000-0003-1135-4253

Armando Peña-Duarte − *Department of Chemistry and Biochemistry, The University of Texas at El Paso, El Paso, Texas 79968, United States;* orcid.org/0000-0002-4286-5278

Huifang Li − *College of Electromechanical Engineering, Qingdao University of Science and Technology, Qingdao, Shandong 266061, China*

Hong Li − *Department of Chemistry and Biochemistry, The University of Arizona, Tucson, Arizona 85721-0088, United States;* orcid.org/0000-0002-4513-3056

Mohamed Fathi Sanad − *Department of Chemistry and Biochemistry, The University of Texas at El Paso, El Paso, Texas 79968, United States*

Pranay Saha − *School of Applied and Interdisciplinary Sciences, Indian Association for the Cultivation of Science, Kolkata 700032, India*

Matthew A. Addicoat − *Department of Chemistry and Forensics, Nottingham Trent University, Clifton Lane, Nottingham NG11 8NS, United Kingdom;* orcid.org/0000-0002-5406-7927

Kotaro Sasaki − *Chemistry Department, Brookhaven National Laboratory, Upton, New York 11973, United States;* orcid.org/0000-0003-2474-8323

T. Amanda Strom − *Materials Research Laboratory and Materials Department, University of California, Santa Barbara, California 93106, United States*

Miguel José Yacamán − *Department of Applied Physics and Materials Science, Northern Arizona University, Flagstaff, Arizona 86011, United States*

Carlos R. Cabrera − *Department of Chemistry and Biochemistry, The University of Texas at El Paso, El Paso, Texas 79968, United States;* orcid.org/0000-0002-3342-8666

Ram Seshadri − *Materials Research Laboratory and Materials Department, University of California, Santa Barbara, California 93106, United States;* orcid.org/0000-0001-5858-4027

https://doi.org/10.1021/acsnano.2c09838
ACS Nano 2023, 17, 3492−3505

Santanu Bhattacharya − *School of Applied and Interdisciplinary Sciences, Indian Association for the Cultivation of Science, Kolkata 700032, India; Department of Organic Chemistry, Indian Institute of Science, Tala Marg, Bangalore 560 012, India;* orcid.org/0000-0001-9040-8971

Jean-Luc Brédas − *Department of Chemistry and Biochemistry, The University of Arizona, Tucson, Arizona 85721-0088, United States;* orcid.org/0000-0001-7278-4471

Complete contact information is available at: https://pubs.acs.org/10.1021/acsnano.2c09838

Funding

National Science Foundation and Robert A. Welch Foundation

Notes

The authors declare no competing financial interest.

ACKNOWLEDGMENTS

L.E. thanks the NSF for the generous support of this work under CHE-1801317. The Robert A. Welch Foundation is also acknowledged for an endowed chair to L.E. (grant AH-0033). The work at the University of Arizona was supported by the UA College of Science. H.F.L acknowledges financial support from the Natural Science Foundation of Shandong Province, China (No. ZR2020MB045). This work was also supported by Center for Alkaline Based Energy Solutions (CABES), an Energy Frontier Research Center funded by the U.S. Department of Energy, Office of Science, Basic Energy Sciences, under award # DESC0019445. C.R.C. acknowledges the STARS Award (2021) of the University of Texas System. This research used beamline 7-BM (QAS) of the National Synchrotron Light Source II, a US DOE Office of Science User Facility operated for the DOE Office of Science by Brookhaven National Laboratory under Contract No. DE-SC0012704. Beamline operations were supported in part by the Synchrotron Catalysis Consortium (US DOE, Office of Basic Energy Sciences, Grant No. DE-SC0012335). The authors appreciate the discussions with S. Ehrlich, L. Ma, and, N. Marinkovic (BNL). The MRL Shared Experimental Facilities are supported by the MRSEC Program of the NSF under Award No. DMR 1720256; a member of the NSF-funded Materials Research Facilities Network (www.mrfn.org). The authors want to also thank J. Nolt (MRL, UC Santa Barbara) for BET analysis. HPC time was granted by the MMM Hub, which is partially funded by EPSRC (EP/T022213).

ABBREVIATIONS USED

HMTA, hexamethylenetetramine; eV, electronvolts; meV, millielectronvolts

REFERENCES

(1) Johnson, L.; Li, C.; Liu, Z.; Chen, Y.; Freunberger, S. A.; Ashok, P. C.; Praveen, B. B.; Dholakia, K.; Tarascon, J.-M.; Bruce, P. G. The Role of LiO_2 Solubility in O_2 Reduction in Aprotic Solvents and its Consequences for Li-O_2 Batteries. *Nat. Chem.* **2014**, *6*, 1091−1099.

(2) Chen, Y.; Qiao, S.; Tang, Y.; Du, Y.; Zhang, D.; Wang, W.; Zhang, H.; Sun, X.; Liu, C. Double-Faced Atomic-Level Engineering of Hollow Carbon Nanofibers As Free-Standing Bifunctional Oxygen Electrocatalysts for Flexible Zn-Air Battery. *ACS Nano* **2022**, *16*, 15273−15285.

(3) Ding, S.; Barr, J. A.; Shi, Q.; Zeng, Y.; Tieu, P.; Lyu, Z.; Fang, L.; Li, T.; Pan, X.; Beckman, S. P.; Du, D.; Lin, H.; Li, J.-C.; Wu, G.; Lin, Y. Engineering Atomic Single Metal-FeN_4Cl Sites with Enhanced Oxygen-Reduction Activity for High-Performance Proton Exchange Membrane Fuel Cells. *ACS Nano* **2022**, *16*, 15165−15174.

(4) Holewinski, A.; Idrobo, J.-C.; Linic, S. High-Performance Ag-Co Alloy Catalysts for Electrochemical Oxygen Reduction. *Nat. Chem.* **2014**, *6*, 828−834.

(5) Yang, L.; Shui, J.; Du, L.; Shao, Y.; Liu, J.; Dai, L.; Hu, Z. Carbon-Based Metal-Free ORR Electrocatalysts for Fuel Cells: Past, Present, and Future. *Adv. Mater.* **2019**, *31*, 1804799.

(6) Sarkar, S.; Biswas, A.; Siddharthan, E. E.; Thapa, R.; Dey, R. S. Strategic Modulation of Target-Specific Isolated Fe,Co Single-Atom Active Sites for Oxygen Electrocatalysis Impacting High Power Zn-Air Battery. *ACS Nano* **2022**, *16*, 7890−7903.

(7) Miner, E. M.; Gul, S.; Ricke, N. D.; Pastor, E.; Yano, J.; Yachandra, V. K.; Van Voorhis, T.; Dincă, M. Mechanistic Evidence for Ligand-Centered Electrocatalytic Oxygen Reduction with the Conductive MOF Ni_3(Hexaiminotriphenylene)$_2$. *ACS Catal.* **2017**, *7*, 7726−7731.

(8) Liu, B.; Feng, R.; Busch, M.; Wang, S.; Wu, H.; Liu, P.; Gu, J.; Bahadoran, A.; Matsumura, D.; Tsuji, T.; Zhang, D.; Song, F.; Liu, Q. Synergistic Hybrid Electrocatalysts of Platinum Alloy and Single-Atom Platinum for an Efficient and Durable Oxygen Reduction Reaction. *ACS Nano* **2022**, *16*, 14121−14133.

(9) You, X.; Cao, L.; Liu, Y.; Wu, H.; Li, R.; Xiao, Q.; Yuan, J.; Zhang, R.; Fan, C.; Wang, X.; Yang, P.; Yang, X.; Ma, Y.; Jiang, Z. Charged Nanochannels in Covalent Organic Framework Membranes Enabling Efficient Ion Exclusion. *ACS Nano* **2022**, *16*, 11781−11791.

(10) Yaghi, O. M. Reticular Chemistry in All Dimensions. *ACS Cent. Sci.* **2019**, *5*, 1295−1300.

(11) She, P.; Qin, Y.; Wang, X.; Zhang, Q. Recent Progress in External-Stimulus-Responsive 2D Covalent Organic Frameworks. *Adv. Mater.* **2022**, *34*, 2101175.

(12) Dey, K.; Mohata, S.; Banerjee, R. Covalent Organic Frameworks and Supramolecular Nano-Synthesis. *ACS Nano* **2021**, *15*, 12723−12740.

(13) Ma, T.; Kapustin, E. A.; Yin, S. X.; Liang, L.; Zhou, Z.; Niu, J.; Li, L.-H.; Wang, Y.; Su, J.; Li, J.; Wang, X.; Wang, W. D.; Wang, W.; Sun, J.; Yaghi, O. M. Single-Crystal X-Ray Diffraction Structures of Covalent Organic Frameworks. *Science* **2018**, *361*, 48−52.

(14) Yaghi, O. M. Reticular Chemistry—Construction, Properties, and Precision Reactions of Frameworks. *J. Am. Chem. Soc.* **2016**, *138*, 15507−15509.

(15) Feng, X.; Ding, X.; Jiang, D. Covalent Organic Frameworks. *Chem. Soc. Rev.* **2012**, *41*, 6010−6022.

(16) Li, H.; Evans, A. M.; Castano, I.; Strauss, M. J.; Dichtel, W. R.; Bredas, J.-L. Nucleation-Elongation Dynamics of Two-Dimensional Covalent Organic Frameworks. *J. Am. Chem. Soc.* **2020**, *142*, 1367−1374.

(17) Evans, A. M.; Castano, I.; Brumberg, A.; Parent, L. R.; Corcos, A. R.; Li, R. L.; Flanders, N. C.; Gosztola, D. J.; Gianneschi, N. C.; Schaller, R. D.; Dichtel, W. R. Emissive Single-Crystalline Boroxine-Linked Colloidal Covalent Organic Frameworks. *J. Am. Chem. Soc.* **2019**, *141*, 19728−19735.

(18) Huang, N.; Wang, P.; Jiang, D. Covalent Organic Frameworks: A Materials Platform for Structural and Functional Designs. *Nat. Rev. Mater.* **2016**, *1*, 16068.

(19) Guo, J.; Jiang, D. Covalent Organic Frameworks for Heterogeneous Catalysis: Principle, Current Status, and Challenges. *ACS Cent. Sci.* **2020**, *6*, 869−879.

(20) You, S.; Gong, X.; Wang, W.; Qi, D.; Wang, X.; Chen, X.; Ren, N. Enhanced Cathodic Oxygen Reduction and Power Production of Microbial Fuel Cell Based on Noble-Metal-Free Electrocatalyst Derived from Metal-Organic Frameworks. *Adv. Energy Mater.* **2016**, *6*, 1501497.

(21) Wang, T. C.; Vermeulen, N. A.; Kim, I. S.; Martinson, A. B. F.; Stoddart, J. F.; Hupp, J. T.; Farha, O. K. Scalable Synthesis and Post-Modification of a Mesoporous Metal-Organic Framework Called NU-1000. *Nat. Protoc.* **2016**, *11*, 149−162.

(22) Chen, T.; Dou, J.-H.; Yang, L.; Sun, C.; Oppenheim, J. J.; Li, J.; Dincă, M. Dimensionality Modulates Electrical Conductivity in Compositionally Constant One-, Two-, and Three-Dimensional Frameworks. *J. Am. Chem. Soc.* **2022**, *144*, 5583−5593.
(23) Kazem-Rostami, M.; Orte, A.; Ortuño, A. M.; David, A. H. G.; Roy, I.; Miguel, D.; Garci, A.; Cruz, C. M.; Stern, C. L.; Cuerva, J. M.; Stoddart, J. F. Helically Chiral Hybrid Cyclodextrin Metal-Organic Framework Exhibiting Circularly Polarized Luminescence. *J. Am. Chem. Soc.* **2022**, *144*, 9380−9389.
(24) Dinakar, B.; Forse, A. C.; Jiang, H. Z. H.; Zhu, Z.; Lee, J.-H.; Kim, E. J.; Parker, S. T.; Pollak, C. J.; Siegelman, R. L.; Milner, P. J.; Reimer, J. A.; Long, J. R. Overcoming Metastable CO_2 Adsorption in a Bulky Diamine-Appended Metal-Organic Framework. *J. Am. Chem. Soc.* **2021**, *143*, 15258−15270.
(25) Fu, Y.; Wu, Y.; Chen, S.; Zhang, W.; Zhang, Y.; Yan, T.; Yang, B.; Ma, H. Zwitterionic Covalent Organic Frameworks: Attractive Porous Host for Gas Separation and Anhydrous Proton Conduction. *ACS Nano* **2021**, *15*, 19743−19755.
(26) Dincă, M.; Long, J. R. Strong H_2 Binding and Selective Gas Adsorption within the Microporous Coordination Solid $Mg_3(O_2C\text{-}C_{10}H_6\text{-}CO_2)_3$. *J. Am. Chem. Soc.* **2005**, *127*, 9376−9377.
(27) Kapelewski, M. T.; Runčevski, T.; Tarver, J. D.; Jiang, H. Z. H.; Hurst, K. E.; Parilla, P. A.; Ayala, A.; Gennett, T.; FitzGerald, S. A.; Brown, C. M.; Long, J. R. Record High Hydrogen Storage Capacity in the Metal-Organic Framework Ni_2(*m*-dobdc) at Near-Ambient Temperatures. *Chem. Mater.* **2018**, *30*, 8179−8189.
(28) Zhi, Y.; Wang, Z.; Zhang, H.-L.; Zhang, Q. Recent Progress in Metal-Free Covalent Organic Frameworks As Heterogeneous Catalysts. *Small* **2020**, *16*, 2001070.
(29) Qian, C.; Zhou, W.; Qiao, J.; Wang, D.; Li, X.; Teo, W. L.; Shi, X.; Wu, H.; Di, J.; Wang, H.; Liu, G.; Gu, L.; Liu, J.; Feng, L.; Liu, Y.; Quek, S. Y.; Loh, K. P.; Zhao, Y. Linkage Engineering by Harnessing Supramolecular Interactions to Fabricate 2D Hydrazone-Linked Covalent Organic Framework Platforms Toward Advanced Catalysis. *J. Am. Chem. Soc.* **2020**, *142*, 18138−18149.
(30) Medina, D. D.; Werner, V.; Auras, F.; Tautz, R.; Dogru, M.; Schuster, J.; Linke, S.; Döblinger, M.; Feldmann, J.; Knochel, P.; Bein, T. Oriented Thin Films of a Benzodithiophene Covalent Organic Framework. *ACS Nano* **2014**, *8*, 4042−4052.
(31) Feng, X.; Liu, L.; Honsho, Y.; Saeki, A.; Seki, S.; Irle, S.; Dong, Y.; Nagai, A.; Jiang, D. High-Rate Charge-Carrier Transport in Porphyrin Covalent Organic Frameworks: Switching from Hole to Electron to Ambipolar Conduction. *Angew. Chem., Int. Ed.* **2012**, *51*, 2618−2622.
(32) Zhang, H.; Sun, W.; Chen, X.; Wang, Y. Few-Layered Fluorinated Triazine-Based Covalent Organic Nanosheets for High-Performance Alkali Organic Batteries. *ACS Nano* **2019**, *13*, 14252−14261.
(33) Yin, C.; Li, Z.; Zhao, D.; Yang, J.; Zhang, Y.; Du, Y.; Wang, Y. Azo-Branched Covalent Organic Framework Thin Films As Active Separators for Superior Sodium-Sulfur Batteries. *ACS Nano* **2022**, *16*, 14178.
(34) Cichocka, M. O.; Liang, Z.; Feng, D.; Back, S.; Siahrostami, S.; Wang, X.; Samperisi, L.; Sun, Y.; Xu, H.; Hedin, N.; Zheng, H.; Zou, X.; Zhou, H.-C.; Huang, Z. A Porphyrinic Zirconium Metal-Organic Framework for Oxygen Reduction Reaction: Tailoring the Spacing between Active-Sites through Chain-Based Inorganic Building Units. *J. Am. Chem. Soc.* **2020**, *142*, 15386−15395.
(35) Jin, Z.; Li, P.; Meng, Y.; Fang, Z.; Xiao, D.; Yu, G. Understanding the Inter-Site Distance Effect in Single-Atom Catalysts for Oxygen Electroreduction. *Nat. Catal.* **2021**, *4*, 615−622.
(36) Wei, S.; Zhang, F.; Zhang, W.; Qiang, P.; Yu, K.; Fu, X.; Wu, D.; Bi, S.; Zhang, F. Semiconducting 2D Triazine-Cored Covalent Organic Frameworks with Unsubstituted Olefin Linkages. *J. Am. Chem. Soc.* **2019**, *141*, 14272−14279.
(37) Cusin, L.; Peng, H.; Ciesielski, A.; Samorì, P. Chemical Conversion and Locking of the Imine Linkage: Enhancing the Functionality of Covalent Organic Frameworks. *Angew. Chem., Int. Ed.* **2021**, *60*, 14236−14250.
(38) Diercks, C. S.; Liu, Y.; Cordova, K. E.; Yaghi, O. M. The Role of Reticular Chemistry in the Design of CO_2 Reduction Catalysts. *Nat. Mater.* **2018**, *17*, 301−307.
(39) Lu, M.; Zhang, M.; Liu, C.-G.; Liu, J.; Shang, L.-J.; Wang, M.; Chang, J.-N.; Li, S.-L.; Lan, Y.-Q. Stable Dioxin-Linked Metallophthalocyanine Covalent Organic Frameworks (COFs) As Photo-Coupled Electrocatalysts for CO_2 Reduction. *Angew. Chem., Int. Ed.* **2021**, *60*, 4864−4871.
(40) Zhu, H.-J.; Lu, M.; Wang, Y.-R.; Yao, S.-J.; Zhang, M.; Kan, Y.-H.; Liu, J.; Chen, Y.; Li, S.-L.; Lan, Y.-Q. Efficient Electron Transmission in Covalent Organic Framework Nanosheets for Highly Active Electrocatalytic Carbon Dioxide Reduction. *Nat. Commun.* **2020**, *11*, 497.
(41) Ma, Y.; Fu, Y.; Jiang, W.; Wu, Y.; Liu, C.; Che, G.; Fang, Q. Excellent Electrocatalytic Performance of Metal-Free Thiophene-Sulfur Covalent Organic Frameworks for Hydrogen Evolution in Alkaline Medium. *J. Mater. Chem. A* **2022**, *10*, 10092−10097.
(42) Clough, A. J.; Yoo, J. W.; Mecklenburg, M. H.; Marinescu, S. C. Two-Dimensional Metal-Organic Surfaces for Efficient Hydrogen Evolution from Water. *J. Am. Chem. Soc.* **2015**, *137*, 118−121.
(43) Aiyappa, H. B.; Thote, J.; Shinde, D. B.; Banerjee, R.; Kurungot, S. Cobalt-Modified Covalent Organic Framework As a Robust Water Oxidation Electrocatalyst. *Chem. Mater.* **2016**, *28*, 4375−4379.
(44) Zhao, X.; Pachfule, P.; Li, S.; Langenhahn, T.; Ye, M.; Schlesiger, C.; Praetz, S.; Schmidt, J.; Thomas, A. Macro/Microporous Covalent Organic Frameworks for Efficient Electrocatalysis. *J. Am. Chem. Soc.* **2019**, *141*, 6623−6630.
(45) Li, D.; Li, C.; Zhang, L.; Li, H.; Zhu, L.; Yang, D.; Fang, Q.; Qiu, S.; Yao, X. Metal-Free Thiophene-Sulfur Covalent Organic Frameworks: Precise and Controllable Synthesis of Catalytic Active Sites for Oxygen Reduction. *J. Am. Chem. Soc.* **2020**, *142*, 8104−8108.
(46) Liang, Z.; Guo, H.; Zhou, G.; Guo, K.; Wang, B.; Lei, H.; Zhang, W.; Zheng, H.; Apfel, U.-P.; Cao, R. Metal-Organic-Framework-Supported Molecular Electrocatalysis for the Oxygen Reduction Reaction. *Angew. Chem., Int. Ed.* **2021**, *60*, 8472−8476.
(47) Tong, Y.; Sun, Z.; Wang, J.; Huang, W.; Zhang, Q. Covalent Organic Framework Containing Dual Redox Centers As an Efficient Anode in Li-Ion Batteries. *SmartMat* **2022**, *3*, 685.
(48) Han, B.; Ding, X.; Yu, B.; Wu, H.; Zhou, W.; Liu, W.; Wei, C.; Chen, B.; Qi, D.; Wang, H.; Wang, K.; Chen, Y.; Chen, B.; Jiang, J. Two-Dimensional Covalent Organic Frameworks with Cobalt(II)-Phthalocyanine Sites for Efficient Electrocatalytic Carbon Dioxide Reduction. *J. Am. Chem. Soc.* **2021**, *143*, 7104−7113.
(49) Zhong, H.; Wang, M.; Ghorbani-Asl, M.; Zhang, J.; Ly, K. H.; Liao, Z.; Chen, G.; Wei, Y.; Biswal, B. P.; Zschech, E.; Weidinger, I. M.; Krasheninnikov, A. V.; Dong, R.; Feng, X. Boosting the Electrocatalytic Conversion of Nitrogen to Ammonia on Metal-Phthalocyanine-Based Two-Dimensional Conjugated Covalent Organic Frameworks. *J. Am. Chem. Soc.* **2021**, *143*, 19992−20000.
(50) Jiang, M.; Han, L.; Peng, P.; Hu, Y.; Xiong, Y.; Mi, C.; Tie, Z.; Xiang, Z.; Jin, Z. Quasi-Phthalocyanine Conjugated Covalent Organic Frameworks with Nitrogen-Coordinated Transition Metal Centers for High-Efficiency Electrocatalytic Ammonia Synthesis. *Nano Lett.* **2022**, *22*, 372−379.
(51) Wu, Q.; Mao, M.-J.; Wu, Q.-J.; Liang, J.; Huang, Y.-B.; Cao, R. Construction of Donor-Acceptor Heterojunctions in Covalent Organic Framework for Enhanced CO_2 Electroreduction. *Small* **2021**, *17*, 2004933.
(52) Chen, W.; Wang, L.; Mo, D.; He, F.; Wen, Z.; Wu, X.; Xu, H.; Chen, L. Modulating Benzothiadiazole-Based Covalent Organic Frameworks Via Halogenation for Enhanced Photocatalytic Water Splitting. *Angew. Chem., Int. Ed.* **2020**, *59*, 16902−16909.
(53) London Metal Exchange (London Metal Exchange). https://www.lme.com/en/metals/ev/lme-cobalt (accessed 2022-09-18).
(54) Yuan, Y.; Wang, J.; Adimi, S.; Shen, H.; Thomas, T.; Ma, R.; Attfield, J. P.; Yang, M. Zirconium Nitride Catalysts Surpass Platinum for Oxygen Reduction. *Nat. Mater.* **2020**, *19*, 282−286.
(55) Sun, T.; Zhao, S.; Chen, W.; Zhai, D.; Dong, J.; Wang, Y.; Zhang, S.; Han, A.; Gu, L.; Yu, R.; Wen, X.; Ren, H.; Xu, L.; Chen, C.;

https://doi.org/10.1021/acsnano.2c09838
ACS Nano 2023, 17, 3492−3505

Peng, Q.; Wang, D.; Li, Y. Single-Atomic Cobalt Sites Embedded in Hierarchically Ordered Porous Nitrogen-Doped Carbon As a Superior Bifunctional Electrocatalyst. *Proc. Natl. Acad. Sci. U. S. A.* **2018**, *115*, 12692−12697.
(56) Shinozaki, K.; Zack, J. W.; Pylypenko, S.; Pivovar, B. S.; Kocha, S. S. Oxygen Reduction Reaction Measurements on Platinum Electrocatalysts Utilizing Rotating Disk Electrode Technique. *J. Electrochem. Soc.* **2015**, *162*, F1384−F1396.
(57) Wan, X.; Wang, H.; Yu, H.; Peng, F. Highly Uniform and Monodisperse Carbon Nanospheres Enriched with Cobalt-Nitrogen Active Sites As a Potential Oxygen Reduction Electrocatalyst. *J. Power Sources* **2017**, *346*, 80−88.
(58) Cheng, W.; Zhao, X.; Su, H.; Tang, F.; Che, W.; Zhang, H.; Liu, Q. Lattice-Strained Metal-Organic-Framework Arrays for Bifunctional Oxygen Electrocatalysis. *Nat. Energy* **2019**, *4*, 115−122.
(59) Ramaswamy, N.; Tylus, U.; Jia, Q.; Mukerjee, S. Activity Descriptor Identification for Oxygen Reduction on Nonprecious Electrocatalysts: Linking Surface Science to Coordination Chemistry. *J. Am. Chem. Soc.* **2013**, *135*, 15443−15449.
(60) Choi, C. H.; Park, S. H.; Woo, S. I. Binary and Ternary Doping of Nitrogen, Boron, and Phosphorus into Carbon for Enhancing Electrochemical Oxygen Reduction Activity. *ACS Nano* **2012**, *6*, 7084−7091.
(61) Lin, Y.; Liu, K.; Chen, K.; Xu, Y.; Li, H.; Hu, J.; Lu, Y.-R.; Chan, T.-S.; Qiu, X.; Fu, J.; Liu, M. Tuning Charge Distribution of FeN_4 Via External N for Enhanced Oxygen Reduction Reaction. *ACS Catal.* **2021**, *11*, 6304−6315.
(62) Liang, J.; Jiao, Y.; Jaroniec, M.; Qiao, S. Z. Sulfur and Nitrogen Dual-Doped Mesoporous Graphene Electrocatalyst for Oxygen Reduction with Synergistically Enhanced Performance. *Angew. Chem., Int. Ed.* **2012**, *51*, 11496−11500.
(63) Han, J.; An, P.; Liu, S.; Zhang, X.; Wang, D.; Yuan, Y.; Guo, J.; Qiu, X.; Hou, K.; Shi, L.; Zhang, Y.; Zhao, S.; Long, C.; Tang, Z. Reordering d Orbital Energies of Single-Site Catalysts for CO_2 Electroreduction. *Angew. Chem., Int. Ed.* **2019**, *58*, 12711−12716.
(64) Huang, X.; Wang, D.; Yan, S.; An, P.; Han, J.; Guo, Z.; Li, X.; Chen, Z.; Chang, L.; Lu, S.; Tang, Z. Copper-Tetracyanoquinodimethane-Derived Copper Electrocatalysts for Highly Selective Carbon Dioxide Reduction to Ethylene. *Nano Res.* **2022**, *15*, 7910−7916.
(65) Han, X.; Zhang, T. Y.; Chen, W. X.; Dong, B.; Meng, G.; Zheng, L. R.; Yang, C.; Sun, X. M.; Zhuang, Z. B.; Wang, D. S.; Han, A. J.; Liu, J. F. Mn-N_4 Oxygen Reduction Electrocatalyst: Operando Investigation of Active Sites and High Performance in Zinc-Air Battery. *Adv. Energy Mater.* **2021**, *11*, 2002753.
(66) Seo, B.; Sa, Y. J.; Woo, J.; Kwon, K.; Park, J.; Shin, T. J.; Jeong, H. Y.; Joo, S. H. Size-Dependent Activity Trends Combined with In Situ X-ray Absorption Spectroscopy Reveal Insights into Cobalt Oxide/Carbon Nanotube-Catalyzed Bifunctional Oxygen Electrocatalysis. *ACS Catal.* **2016**, *6*, 4347−4355.
(67) Lien, H.-T.; Chang, S.-T.; Chen, P.-T.; Wong, D. P.; Chang, Y. C.; Lu, Y.-R.; Dong, C.-L.; Wang, C.-H.; Chen, K.-H.; Chen, L.-C. Probing the Active Site in Single-Atom Oxygen Reduction Catalysts Via Operando X-Ray and Electrochemical Spectroscopy. *Nat. Commun.* **2020**, *11*, 4233.
(68) Zhang, X.; Xu, X.; Yao, S.; Hao, C.; Pan, C.; Xiang, X.; Tian, Z. Q.; Shen, P. K.; Shao, Z.; Jiang, S. P. Boosting Electrocatalytic Activity of Single Atom Catalysts Supported on Nitrogen-Doped Carbon through N Coordination Environment Engineering. *Small* **2022**, *18*, 2105329.
(69) Guo, J.; Lin, C.-Y.; Xia, Z.; Xiang, Z. A Pyrolysis-Free Covalent Organic Polymer for Oxygen Reduction. *Angew. Chem., Int. Ed.* **2018**, *57*, 12567−12572.
(70) Soto-Pérez, J.; Betancourt, L. E.; Trinidad, P.; Larios, E.; Rojas-Pérez, A.; Quintana, G.; Sasaki, K.; Pollock, C. J.; Debefve, L. M.; Cabrera, C. R. In Situ X-Ray Absorption Spectroscopy of PtNiNanowire/Vulcan XC-72R Under Oxygen Reduction Reaction in Alkaline Media. *ACS Omega* **2021**, *6*, 17203−17216.
(71) Addicoat, M. A.; Coupry, D. E.; Heine, T. AuToGraFS: Automatic Topological Generator for Framework Structures. *J. Phys. Chem. A* **2014**, *118*, 9607−9614.
(72) Addicoat, M. A.; Vankova, N.; Akter, I. F.; Heine, T. Extension of the Universal Force Field to Metal-Organic Frameworks. *J. Chem. Theory Comput.* **2014**, *10*, 880−891.
(73) Coupry, D. E.; Addicoat, M. A.; Heine, T. Extension of the Universal Force Field for Metal-Organic Frameworks. *J. Chem. Theory Comput.* **2016**, *12*, 5215−5225.
(74) Grimme, S.; Bannwarth, C.; Shushkov, P. A Robust and Accurate Tight-Binding Quantum Chemical Method for Structures, Vibrational Frequencies, and Noncovalent Interactions of Large Molecular Systems Parametrized for All Spd-Block Elements (Z = 1−86). *J. Chem. Theory Comput.* **2017**, *13*, 1989−2009.
(75) Rüger, R.; Franchini, M.; Trnka, T.; Yakovlev, A.; Lenthe, E. v.; Philipsen, P.; Vuren, T. v.; Klumpers, B.; Soini, T.*AMS 2022.1; SCM, Theoretical Chemistry*; Vrije Universiteit: Amsterdam, The Netherlands. http://www.scm.com (accessed 2022-09-15).
(76) Blöchl, P. E. Projector Augmented-Wave Method. *Phys. Rev. B* **1994**, *50*, 17953−17979.
(77) Kresse, G.; Furthmüller, J. Efficiency of Ab-initio Total Energy Calculations for Metals and Semiconductors using a Plane-Wave Basis Set. *Comput. Mater. Sci.* **1996**, *6*, 15−50.
(78) Kresse, G.; Furthmüller, J. Efficient iterative schemes for Ab Initio Total-energy Calculations Using a Plane-Wave Basis Set. *Phys. Rev. B* **1996**, *54*, 11169−11186.
(79) Perdew, J. P.; Burke, K.; Ernzerhof, M. Generalized Gradient Approximation Made Simple. *Phys. Rev. Lett.* **1996**, *77*, 3865−3868.
(80) Grimme, S. Semiempirical GGA-type Density Functional Constructed with a Long-Range Dispersion Correction. *J. Comput. Chem.* **2006**, *27*, 1787−1799.
(81) Hermanns, C. F.; Tarafder, K.; Bernien, M.; Krüger, A.; Chang, Y.-M.; Oppeneer, P. M.; Kuch, W. Magnetic Coupling of Porphyrin Molecules Through Graphene. *Adv. Mater.* **2013**, *25*, 3473−3477.
(82) Monkhorst, H. J.; Pack, J. D. Special Points for Brillouin-Zone Integrations. *Phys. Rev. B* **1976**, *13*, 5188−5192.
(83) Kitchin, J. R.; Nørskov, J. K.; Barteau, M. A.; Chen, J. G. Modification of the Surface Electronic and Chemical Properties of Pt (111) by Subsurface 3d Transition Metals. *J. Chem. Phys.* **2004**, *120*, 10240−10246.
(84) Nørskov, J. K.; Rossmeisl, J.; Logadottir, A.; Lindqvist, L.; Kitchin, J. R.; Bligaard, T.; Jónsson, H. Origin of the Overpotential for Oxygen Reduction at a Fuel-Cell Cathode. *J. Phys. Chem. B* **2004**, *108*, 17886−17892.
(85) Wang, V.; Xu, N. VASPKIT: A Pre- and Post-Processing Program for the VASP Code. *Computer Physics Communications* **2021**, 108033.
(86) Yang, N.; Zheng, X.; Li, L.; Li, J.; Wei, Z. Influence of Phosphorus Configuration on Electronic Structure and Oxygen Reduction Reactions of Phosphorus-Doped Graphene. *J. Phys. Chem. C* **2017**, *121*, 19321−19328.
(87) Deng, Q.; Zhao, J.; Wu, T.; Chen, G.; Hansen, H. A.; Vegge, T. 2D Transition Metal-TCNQ Sheets As Bifunctional Single-Atom Catalysts for Oxygen Reduction and Evolution Reaction (ORR/OER). *J. Catal.* **2019**, *370*, 378−384.
(88) Chai, J.-D.; Head-Gordon, M. Long-Range Corrected Hybrid Density Functionals with Damped Atom-Atom Dispersion Corrections. *Phys. Chem. Chem. Phys.* **2008**, *10*, 6615−6620.
(89) Frisch, M. J.; Trucks, G. W.; Schlegel, H. B.; Scuseria, G. E.; Robb, M. A.; Cheeseman, J. R.; Scalmani, G.; Barone, V.; Mennucci, B.; Petersson, G. A.; et al.*Gaussian 09*, Revision D.01; Gaussian, Inc.: Wallingford, CT, 2013.
(90) Andrae, D.; Hässermann, U.; Dolg, M.; Stoll, H.; Preuss, H. Energy-Adjusted ab Initio Pseudopotentials for the Second and Third Row Transition Elements. *Theor. Chim. Acta.* **1990**, *77*, 123−141.
(91) Hehre, W. J.; Ditchfield, R.; Pople, J. A. Self-Consistent Molecular Orbital Methods. XII. Further Extensions of Gaussian-type Basis Sets for use in Molecular Orbital Studies of Organic Molecules. *J. Chem. Phys.* **1972**, *56*, 2257−2261.

https://doi.org/10.1021/acsnano.2c09838
ACS Nano 2023, 17, 3492−3505

(92) Francl, M. M.; Pietro, W. J.; Hehre, W. J.; Binkley, J. S.; Gordon, M. S.; DeFrees, D. J.; Pople, J. A. Self-Consistent Molecular Orbital Methods. XXIII. A Polarization-Type Basis Set for Second-Row Elements. *J. Chem. Phys.* **1982**, *77*, 3654−3665.

Recommended by ACS

Three-Component Donor−π−Acceptor Covalent–Organic Frameworks for Boosting Photocatalytic Hydrogen Evolution

Ziping Li, Xiaoming Liu, *et al.*
MARCH 14, 2023
JOURNAL OF THE AMERICAN CHEMICAL SOCIETY READ

Phenanthroimidazole-Based Covalent Organic Frameworks with Enhanced Activity for the Photocatalytic Hydrogen Evolution Reaction

Cong-Xue Liu, Eunsung Lee, *et al.*
JANUARY 06, 2023
ACS APPLIED ENERGY MATERIALS READ

Post-synthetic Fully π-Conjugated Three-Dimensional Covalent Organic Frameworks for High-Performance Lithium Storage

Renzeng Chen, Yingjie Zhao, *et al.*
DECEMBER 30, 2022
ACS APPLIED MATERIALS & INTERFACES READ

Janus Dione-Based Conjugated Covalent Organic Frameworks with High Conductivity as Superior Cathode Materials

Xiaoyi Xu, Ning Huang, *et al.*
DECEMBER 30, 2022
JOURNAL OF THE AMERICAN CHEMICAL SOCIETY READ

Get More Suggestions >

https://doi.org/10.1021/acsnano.2c09838
ACS Nano 2023, 17, 3492−3505